

# Flow and Mixing Performance in Helical Ribbon Mixers

Martin Robinson<sup>1</sup> and Paul W. Cleary

CSIRO Mathematics, Informatics and Statistics  
Private Bag 33, Clayton South, Vic, 3168. Australia  
E-mail: [firstname.lastname@csiro.au](mailto:firstname.lastname@csiro.au)

## Abstract

This paper explores the effect of impeller design on the chaotic mixing in a helical ribbon mixer. Numerical simulations using the Smoothed Particle Hydrodynamics (SPH) method are used to solve for the fluid flow around the moving impellor. The mixing flow is visualised by extracting the hyperbolic Lagrangian Coherent Structures (LCS) of the flow from the Finite-Time Lyapunov Exponent (FTLE) field, which provides qualitative information about the topology of the mixing structures and highlights the major barriers to transport. This is combined with a mixing measure that calculates the degree of mixing between different regions. A single helical ribbon mixer (SHR) was found to create an axially symmetric circulation cell that moves fluid down the outside of the tank and upward near the centre. Smaller circulation cells near the inside edge of the ribbon superimpose a chaotic mixing flow over this primary flow, which stretches and folds fluid volumes around the ribbon according to the shape of the LCSs. The horizontal struts supporting the ribbon generate strong circumferential mixing, but this is only within a narrow horizontal plane with thickness comparable with the strut diameter. The addition of an extra ribbon, 180 degrees out of phase (DHR) doubles the number of smaller circulation cells while decreasing their efficiency in mixing the fluid between the inner and outer regions of the tank. Overall the mixing rate is improved over the other ribbon geometries. The

---

<sup>1</sup> **Corresponding author**

**Current Address:**

Multiscale Mechanics group, Faculty of Engineering Technology  
University of Twente, P.O. Box 217, 7500 AE Enschede, Netherlands  
E-mail: [m.j.robinson@ctw.utwente.nl](mailto:m.j.robinson@ctw.utwente.nl)  
phone: +31 53 4893061

addition of a central screw (CSR) creates a zone of low mixing immediately surrounding the screw. The mixing processes surrounding the helical ribbon are qualitatively identical to the SHR, but the overall mixing rate is slightly increased.

**Key words:**

Helical Ribbon Mixer; Chaotic Advection; Lagrangian Coherent Structures; Mixing; Smoothed Particle Hydrodynamics, SPH; Numerical analysis; Simulation; Transport processes; Visualisation

## **Introduction**

The efficient mixing of a highly viscous fluid is important in many industrial processes, e.g. the production of paints, polymers or food. Achieving efficient and homogenous mixing is challenging at these low Reynolds numbers, due to the increased power needed to move the viscous fluid around the mixer and the laminar nature of the flow.

The Helical Ribbon batch mixer is often used for low Reynolds number industrial mixing. It consists of one or more helical ribbons that wind around a central rotating shaft, usually supported by cross-beams. A separate helical screw can also be wound around the central shaft.

This paper explores the mixing characteristics of the chaotic flow within this class of industrial mixer. While the velocity field itself is laminar, its stretching and folding actions of the velocity field on the fluid means that the trajectory of any Lagrangian point in the flow can be chaotic, which is essential in any mixing process that does not rely on diffusion (Metcalf et al. 2006, 2010).

To investigate the effect of impellor geometry on the mixing, three impellor geometries are considered and compared with each other; a single helical ribbon (SHR), a double helical ribbon (DHR) and a single helical ribbon with a central screw (CSR). The aim of this paper is to investigate, using numerical simulation, the link between the impellor geometry and the structure of the chaotic mixing processes.

Practical mixer designs are usually the result of trial and error. Mixers are normally evaluated using measurements (e.g. circulation time) taken at arbitrary locations in the mixer. This does not give an understanding of the spatial distribution or the topological nature of the transport processes, making the efficient optimisation of the mixer design difficult.

Numerical simulations have a greater flexibility in analysing and visualising the mixing. In two-dimensions, the advection of coloured tracer particles or the spatial distribution of length stretch can provide insight into the spatial variation in the mixing. However, these methods are difficult to visualise and use effectively in three dimensions.

Recently, the concept of a Lagrangian Coherent Structure (LCS) was proposed by Haller and Yuan (2000). This is a finite-time version of a hyperbolic invariant manifold, a two dimensional Lagrangian surface within a chaotic flow that separates regions with very different mixing characteristics. In a steady flow, such as the flows discussed in this paper, the hyperbolic LCS are normally the stable and unstable hyperbolic invariant manifolds of the flow and so techniques used to calculate the LCSs can also be used to find the invariant manifolds. These manifolds originate from hyperbolic fixed points or periodic orbits in the flow, points that are also associated with strong stretching and folding of fluid regions. The manifolds show the topological structure of these mixing actions. Since they are material surfaces that are advected along with the flow, these manifolds can also delineate regions that are isolated to some degree from the surrounding flow and therefore slow to mix with the rest of the domain. For more background on mixing and chaos in dynamical systems, consult books by Ottino (1989) or Wiggins (1992).

LCSs and invariant manifolds have been used to study two dimensional flows in the atmosphere (Pierrehumbert and Yang, 1993), ocean (Shadden et al. 2005) or even biological cell evolution (Aldridge et al. 2006). Sadlo and Peikert (2009) have previously shown a technique for extracting the LCSs from three dimensional grid-based simulations, but only demonstrated their technique for a few example flows and did not use the resultant surfaces to provide any mixing or flow analysis. Previously, Robinson et al. (2008, 2010) used SPH, a particle-based method, to simulate the flow within a Twin Cam mixer in two dimensions. The hyperbolic LCSs (or invariant manifolds, since the flow is periodic around the mixer) of the flow were calculated from the SPH data and used to explore the effects of different impellor geometry and operating conditions. In this case, the manifold structure provided good insight into the mixing processes and highlighted regions of poor mixing in the flow. Here we continue this work, and extend the method to three dimensions and use this to explore the mixing behaviour of one of the most common forms of industrial fluid mixers. The transition of this analysis to three dimensions presents significant computational and visualisation challenges. This paper demonstrates that SPH simulation of fluid flow and mixing in these types of process equipment is feasible and shows that the LCS methodology can be used to gain insight into the chaotic transport within three dimensional industrial mixers. The hyperbolic LCSs extracted from the SPH

simulations are used to perform a study of the effect of impellor geometry, combining the qualitative information given by the manifolds with a quantitative mixing measure in order to rigorously compare the different mixing flow around each impellor.

The calculation of LCS surfaces in 3D flows has been demonstrated in (Sadlo and Peikert, 2009) and (Lipinski and Mohseni, 2010), but both use an Eulerian grid to represent the flow and require the advection of large numbers of tracer particles. Lipinsky and Mohseni (2010) reduce the number of tracers by only calculating the FTLE field near the manifolds, but instead require the full flow field from  $t = t_0$  to  $t = t_0 + T$  (resolved in both time and space) to be stored in memory. Conversely, the method described in this paper uses Lagrangian particle data to represent the flow field, and the full FTLE field can be calculated with only  $O(M \log N)$  complexity (where  $N$  is the number of particles) using only the particle positions at the beginning and end of the time period. This significantly reduces the computational burden needed to calculate the LCSs.

The Smoothed Particle Hydrodynamics (SPH) (Monaghan, 2005) method is used for the numerical simulations presented in this paper. SPH is a Lagrangian particle method for simulating fluid flow. Rather than using a fixed grid, the fluid variables are interpolated over a disordered set of particles which move with the fluid velocity. Each particle represents a volume of fluid, so it can have its own physical properties and the advection is obtained automatically from the motion of the particles. Unlike grid-based methods, the time history of each particle is readily available using SPH. This greatly simplifies the calculation of the LCSs and eliminates the need to integrate large numbers of tracer particles in the flow.

The SPH code used in this paper has been previously validated against experimental data of a 3D dam break against a rigid column (Cummins et. al. 2012), and the mixing of large particulate solids (Cleary et. al. 2007). The authors have used an identical SPH method to simulate a 2D twin cam mixer and validate against FEM and experimental results (Robinson et. al. 2008). Other more general validation results, using the same weakly compressible SPH formulation used in this paper, can be seen in (Colagrossi and Landrini 2003), who simulate an air-water interface in bubbles and waves, and (Khayyera and Gotoha 2010), who validate a simulation of a dam break over a wet bed.

There have been a number of prior experimental and computational studies of the Helical Ribbon mixer. Delaplace et al. (2000) has compiled a review of the experimental literature for helical ribbon mixers. The mixers were compared using circulation and mixing time. While Delaplace does not give an ideal geometry, a region of the parameter space is defined that results in an acceptable rate of mixing. The helical ribbon parameters used in this paper fall in this region and match the experiments performed by Guerin et al. (1984), who presented data for the circulation times and distributions taken at different regions in the mixing tank. They are also similar to the parameters used by Carreau et al. (1976) (provides circulation and mixing times) and Patterson et al. (1979) (provides power consumption). However, these experimental studies were only able to characterise the global mixing using measures that do not directly measure the mixing (circulation times) or are only qualitative in nature (mixing times). They do not provide information on the structure of the local mixing and transport characteristics of the flow, the degree to which they are optimal or otherwise, nor how these are affected by changes in geometry or operating conditions.

Numerical simulation can provide much more details of the internal structure of the flow dynamics. Tanguy et al (1992, 1997) have therefore performed simulations of Helical Ribbon mixers using the Finite Element method (FEM). However, their analysis of the mixing was limited to providing circulation times and tracer trajectories for a few different positions in the mixer. De La Villeon et al. (1998) presented results from a FEM simulation of three different helical ribbon geometries qualitatively similar to those used in this paper. Villeon et al. provide a more detailed analysis of the mixing, but largely focused on one or two arbitrary points in the flow, calculating the Finite Time Lyapunov Exponent (FTLE) and the dispersion of tracers initially located at these points. However, we will show that the FTLE field, and hence the mixing, varies considerably over the domain. Therefore the results by Villeon et al. could vary significantly with positions of the points used for analysis.

In contrast to the grid-based methods that have been utilised by Tanguy et al. (1997) and Villeon et al. (1998), the SPH method provides Lagrangian particle position data at each timestep in the flow. This eliminates the need to advect large number of tracer

particles in the flow and significantly simplifies the post-processing analysis of mixing flows.

As shown in this paper, SPH data can be used to immediately:

1. visualise the transport of arbitrary fluid volumes to see how they are stretched and folded by the impellor action
2. calculate FTLE data at every point in the domain, which can in turn be used to visualise the mixing structures (i.e. the LCSs) that are present in the flow.

This enables a much more detailed study of the mixing processes in the simulated flow.

## **1 Helical Ribbon Mixer: configuration and impellers**

The base structure of the mixer is a cylindrical tank with diameter  $D = 144$  mm, containing a rotating Helical Ribbon impellor. The flow field around three primary helical ribbon impellor configurations have been simulated using the SPH method. The three impellers are shown in Figure 1 and are specified as follows:

1. A single helical ribbon (SHR) with diameter  $d = 130$  mm, pitch  $p = 0.72d$ , width  $w = 0.1d$  and depth  $0.023d$ . The ribbon is attached to a central cylindrical shaft with diameter  $0.1d$  and is supported by two cylindrical arms with diameter  $0.05d$ .
2. A double helical ribbon (DHR) with identical parameters to the SHR. The two ribbons are 180 degrees out of phase with each other.
3. A single helical ribbon with a central screw (CSR). The single helical ribbon has identical parameters as the SHR. The central screw winds around the central shaft and the cross-sectional area has a width and depth equal to the outer ribbon. The screw pitch is equal in magnitude to the outer ribbon but has an opposite sign.

In all the simulations reported here, the angular velocity of the impeller is  $\omega = 1$  and the viscosity of the fluid is set so that the Reynolds number is  $\text{Re} < 10$ . It is well

known (Delaplace et al. 2000) that the global mixing characteristics of a helical ribbon mixer are independent of  $Re$  for a laminar flow. Chavan et al. (1973) found that  $\omega t_c$ , where  $t_c$  is the average circulation time and  $\omega$  is the impeller rotation speed, was constant for  $Re < 10$ . Chavan and Ulbrecht (1975) found that  $\omega t_m$ , where  $t_m$  is the mixing time, is also constant for  $Re < 10$ .

The viscosity used for the simulations is  $\nu = 2.1 \times 10^{-3} \text{ m}^2/\text{s}$ , which gives a Reynolds number of  $Re = 2$ , using the velocity of the ribbon as the characteristic velocity and the radius of the ribbon as the characteristic length. Given that  $Re < 10$ , the flow solution will be representative of the flow for all lower Reynolds numbers.

## **2 Hyperbolic Invariant Manifolds, Lagrangian Coherent Structures and Mixing**

In periodic flows that exhibit chaotic trajectories, the stable and unstable hyperbolic invariant manifolds provide a useful description of the transport properties of the flow. These manifolds are Lagrangian structures that originate from hyperbolic fixed points or periodic orbits in the flow. They show the topological structure of the stretching and folding actions that generate mixing.

The non-periodic equivalents to stable and unstable manifolds are hyperbolic Lagrangian Coherent Structures (LCSs). These are not necessarily tied to fixed points or periodic orbits and are surfaces that either attract or repel neighbouring material trajectories at a locally maximum rate. As the flows considered in this paper are all steady in time, hyperbolic LCS and stable/unstable manifolds are equivalent.

There are two different types of hyperbolic invariant manifolds, *stable* and *unstable*.

- Lagrangian points on a stable manifold will approach each other and the manifold's hyperbolic point as  $t \rightarrow \infty$ . Points near the manifold will move exponentially away from the manifold with time. This is shown in Figure 2. For this reason, a stable manifold will also be referred to as a *repelling* manifold.
- In contrast, Lagrangian points on an unstable manifold will move away from each other and the hyperbolic point over time. Their motion is most easily

understood by considering the flow when time is reversed. In this time-reversed case, Lagrangian points on an unstable manifold approach the manifold's hyperbolic point as  $t \rightarrow -\infty$ . Nearby points will approach the manifold over time (see Figure 2), and therefore it will be referred to as an *attracting* manifold.

The intersection of an attracting and repelling manifold is a region of strong mixing in the flow. As shown in Figure 2, fluid volumes approaching this point (or line in three dimensions) are stretched tangentially away from the repelling/stable manifold and are folded along the length of the attracting/unstable manifold. The manifold geometry therefore determines the nature of the mixing flow and its overall level of efficiency. Identifying the manifolds and their intersection can provide important qualitative information on the structural nature of the mixing actions.

The attracting and repelling manifolds are Lagrangian surfaces in the flow. Since they are advected with the flow, the flux of fluid across each manifold is zero and they can therefore delineate regions in the flow that are isolated from each other. Manifolds occur in pairs originating from the same hyperbolic point, one attracting and one repelling, and these can also interact to delineate regions that only have a small flux of fluid between them.

As an example, consider the situation in Figure 3, which depicts, in two dimensions, a pair (also known as a tangle) of attracting and repelling manifolds in a periodic flow. This tangle of manifolds separates two regions of fluid at the top and bottom of the figure. The main fluid flow is moving from left to right, but there is a small flux of fluid across the manifold barrier. Each manifold is a Lagrangian structure and therefore moves with the velocity of the fluid. As described (see the manifold properties listed above), points on the attracting manifold will approach each other over time and a line of fluid coincident with the attracting manifold will therefore contract over time. In the opposite manner, a line of fluid coincident with the repelling manifold expands. Consider the motion of the grey lobe of fluid in the far left of Figure 3. As the attracting manifold contracts the upper boundary of this lobe of fluid will move downward, and the expansion of the repelling manifold will allow the lower boundary of the lobe to be stretched out into the lower fluid region. Therefore,

due to the combination of contraction and expansion of the surrounding manifolds, this lobe of fluid will be moved from one side of the manifold tangle to the other.

The rate of fluid transport across the tangle of manifolds is proportional to the area of the lobes. Wide manifold tangles, where the attracting and repelling manifolds are well separated, generate greater mixing than tangles that contain closely spaced or nearly co-incident manifolds. Therefore, the geometry of the manifolds and the area of the lobes between them are an important characteristic of any mixing flow. At the extreme, coincident manifold pairs will act as strong barriers to transport and will lead to the formation of dead zones in the mixer. Even manifold pairs that are close to coincident (i.e. intersect each other with very low angles of incidence) will only allow a small flux of fluid across their length, which will restrict mixing between these regions.

In three dimensions, the manifolds are complex surfaces and their visualisation and interpretation is much more difficult. However, they still control the mixing performance and so still need to be identified and understood. There are two manifold properties that are most important in terms of evaluating the quality of mixing within an industrial device. Firstly, points or lines of manifold intersection highlight regions of strong hyperbolic flow, which is important for good mixing since fluid volumes in these regions undergo strong stretching and folding. An ideal mixer would have manifolds and intersection points that are uniformly distributed throughout the domain. Secondly, any manifold pair that is co-incident, or close to coincident, represent a strong barrier to mixing. If such a structure is persistent throughout the period of the flow then it leads to the formation of two distinct regions between which mixing will be slow (Robinson et al. 2008).

### **3 Calculation of 3D Lagrangian Coherent Structures**

This section describes a new method which was developed for calculating the 3D hyperbolic LCSs in finite-time fluid flows using SPH particle data. For the steady flows described in this paper, the LCSs will correspond to the hyperbolic invariant manifolds. This process is best performed using a Lagrangian particle method such as SPH since there is no need to track Lagrangian tracers through the time varying solution and eliminates any numerical diffusion resulting from the interpolation of the

velocity field. In order to calculate the manifold structure, SPH data from only two timesteps is needed, separated by some characteristic time  $T$  (the period of the mixer in this case). This is significantly more efficient than grid-based simulations, where sufficiently time-resolved velocity data over the entire time period  $T$ , needs to be stored in order to integrate the trajectories of large numbers of tracer particles.

### **3.1 Finite-Time Lyapunov Exponents**

The geometry of the repelling and attracting manifolds can be found by calculating the spatial distribution of the Finite-Time Lyapunov Exponents (FTLE) (Haller 2001, 2002; Shadden et al. 2005). A repelling manifold will normally appear in this field as a maximum ridge in the forward time FTLE field. Here a ridge is defined as a surface whose points are local maxima, in at least one dimension, of the three-dimensional FTLE field. Similarly, an attracting manifold will normally produce a maximum ridge in the backwards time FTLE field.

However, care must be taken as there are some cases where either (a) ridges in the FTLE field do not always correspond to LCS manifolds or (b) LCSs do not always produce ridges in the FTLE field. The most common case is regions of high shear, which produce maximum ridges in the FTLE field with no corresponding LCS. Haller (2011) explores this discrepancy further and provides other, non-shear flow examples where the FTLE field is not sufficient to calculate the LCSs. Haller (2011) goes on to propose a more rigorous method of LCS calculation, which we have attempted to implement but found the resultant manifolds to be too fragmented to be useful. However, the coincidence of maximum ridges in the FTLE field and LCSs has been used successfully in many studies using both numerical and experimental flow (Pierrehumbert and Yang, 1993; Shadden et al. 2005; Aldridge et al. 2006; Sadlo and Peikert 2009; Robinson et al. 2010). Therefore we will follow this example and assume that attracting and repelling LCS manifolds correspond to ridges in the FTLE field, except for obvious regions of high shear (e.g. near no-slip boundaries).

In order to calculate the FTLE field, consider a line segment at time  $t$  with length vector  $\mathbf{dx}$  that moves with the flow velocity. Assume that this segment is aligned along the direction of maximum stretching of the flow. At time  $t+T$  this length has

moved to a new orientation and length  $\mathbf{dX}$ . The FTLE measures the exponential stretching of  $\mathbf{dx}$  over time  $T$ .

$$\sigma = \lim_{\|\mathbf{dx}\| \rightarrow 0} \frac{1}{T} \ln \frac{\|\mathbf{dX}\|}{\|\mathbf{dx}\|} \quad (1)$$

The forwards time FTLE field is calculated using a positive value of  $T$ , whereas the backwards time FTLE field integrates backwards in time.

The relative stretching of the line segments  $\mathbf{dx}$  and  $\mathbf{dX}$  can be found using the right Cauchy-Green deformation tensor  $\mathbf{C}$ ,

$$\|\mathbf{dX}\|^2 = \mathbf{dx} \cdot \mathbf{C} \mathbf{dx} \quad (2)$$

The maximum eigenvalue of  $\mathbf{C}$ ,  $\lambda_{max}$ , is therefore equal to the squared stretching ratio

$$\lambda_{max} = \frac{\|\mathbf{dX}\|^2}{\|\bar{\mathbf{dx}}\|^2} \quad (3)$$

where the bar over  $\mathbf{dx}$  indicates that it is aligned with the eigenvector corresponding to  $\lambda_{max}$ .

Using Eq. (1) the Finite-Time Lyapunov Exponent  $\sigma$  is therefore

$$\sigma = \frac{1}{T} \ln \left( \sqrt{\lambda_{max}} \right) \quad (4)$$

The limit of  $\|\mathbf{dx}\|$  in (1) remains, and is reflected in the resolution of the numerical solution for the flow field, which should also approach zero.

Grid-based numerical methods normally use tracers to calculate the FTLE (Shadden et al. 2005). The tracers are initialised on a regular grid, which simplifies the estimation of the deformation tensor  $\mathbf{C}$ . For the Lagrangian SPH method, the SPH particles move with the local flow velocity and can be used in place of tracers. However, they will typically not be regularly spaced, so a least-squares method has been developed (Robinson et al. 2008) to calculate the deformation gradient, whereby a linear fit of the deformation gradient is performed using the relative positions of all

the neighbouring particles (i.e. all particles at a distance of  $2h$  from the base particle, where  $h$  is the SPH kernel smoothing length and can be regarded as the minimum resolution of the SPH simulation).

### **3.2 Three-Dimensional Ridge Detection**

A new method is proposed for automatically extracting the hyperbolic LCS manifolds from a 3D FTLE field that was calculated on the (irregularly spaced) SPH particles. This is based on a ridge detection method originally developed for image processing by Haralick (1983). As explained previously, repelling/attracting manifolds will appear as ridges in the forward/backwards time FTLE field.

Haralick defined a ridge in a 2D function  $L$  as the maxima of  $L$  along the direction given by the greatest magnitude of  $L$ 's second order directional derivative. In other words, if  $H$  is the Hessian of  $L$ ,  $\lambda_H$  is the eigenvalue of  $H$  with the greatest magnitude and  $\mathbf{v}_H$  is the corresponding eigenvector, then Harilick's definition of a ridge is a line whose points satisfy

$$\lambda_H < 0 \quad (5)$$

$$\nabla L \cdot \mathbf{v}_H = 0 \quad (6)$$

This definition was extended to  $n$  dimensions by Eberly (1996). Let  $\lambda_1 \leq \lambda_2 \leq \dots \leq \lambda_n$  be the  $n$  ordered (signed order) eigenvalues of  $H$  and  $\mathbf{v}_i$  the unit eigenvector corresponding to  $\lambda_i$ . All the points on a  $k$ -dimensional ridge will satisfy

$$\lambda_{n-k} < 0 \quad (7)$$

$$\nabla L \cdot \mathbf{v}_i = 0 \text{ for } i = 1, 2, \dots, n-k \quad (8)$$

We are interested in finding a  $k = 2$  dimensional ridge in an  $n = 3$  dimensional function.

In order to calculate the gradient and Hessian of the FTLE field  $\sigma$ , we have used the Symmetric SPH (SSPH) interpolation scheme proposed by Zhang and Batra (2009). This scheme provides a method of estimating any of the first  $m$  derivatives of a given

particle variable. The SSPH method is based around the expansion of the function around each particle using a Taylor series. If the first  $n$  terms of the Taylor series are used, the SSPH estimate of the  $i^{\text{th}}$  derivative is consistent up to order  $(n-i)$ . As we are interested in finding the 2<sup>nd</sup> derivatives of the FTLE field, we use the first three terms of the Taylor series and thus ensure consistent results (irrespective of SPH particle arrangement) for linear FTLE fields. More accurate results might be obtained from using more terms of the Taylor series, but this was not explored as this would require the inversion of an  $(n! \times n!)$  matrix.

Using the SSPH method, the Hessian and gradient of  $\sigma$  is calculated at locations in a regular grid of points that span the domain of the SPH simulation. The left hand side of Equation (8) is then evaluated at each point (taking  $L(x,y) = \sigma(x,y)$ ), and the zero-crossings of this function are determined using a standard Marching Cubes algorithm (Lorensen and Cline, 1987). The resultant surfaces are the potential manifolds.

Once the potential manifolds are extracted from the data, they are ranked using a measure of ridge strength  $S(\mathbf{x})$  proposed by Lindburg (1996).

$$S(x) = |\lambda_1| \quad (9)$$

This function is interpolated at each node of each surface using a standard SPH interpolation function. Each surface is then given a score equal to the sum of the ridge strength over all its nodes. Note that the manifolds returned by the Marching Cubes algorithm are surfaces in the form of an unconnected triangular mesh and these must first be connected to create surfaces before the manifold score can be calculated. A pair of elements that share an edge is deemed to be connected if the angle between them  $\alpha$  is sufficiently small. This angle limit will depend on the resolution of the simulation and the maximum curvature of the manifold. We have used  $\alpha < 37$  degrees for all the results presented in this paper.

This method results in a set of ranked surfaces. The surfaces with the highest scores are the largest and most dominant manifolds of the flow. The surfaces with lower scores are smaller, less important manifolds and surfaces that arise due to errors in the flow solution or in the extraction of the manifolds. The scores for these erroneous surfaces are almost always far below those of the true manifolds and are easily

removed. If errors do occur in the flow solution or manifold extraction, they do not alter the basic structure of the manifolds but instead tend to fragment the representation of the extracted manifold.

It is important that areas near the boundaries are sufficiently resolved to capture the manifold structure since these are typically regions of higher shear which contributes to generating mixing structures. The SPH kernel is not be fully supported by particles at distances less than two particle spacings from these boundaries, which introduces errors into the Hessian and FTLE gradient interpolations. In our implementation, these gradients are corrected using the SSPH method with  $n = 3$ , which ensures that the gradient of a polynomial FTLE field with degree less than 3 will be calculated correctly, irrespective of the positions of the particles.

### **3.3 Quantification of mixing**

The manifold geometry provides qualitative insight into the structure of the mixing flows within the Helical Ribbon mixer. However, a quantitative measure of mixing is also needed in order to provide a rigorous comparison of the impellers studied here. We use a mixing measure  $M(\mathbf{x})$  described in (Robinson et al. 2008), which provides a measure of the degree to which an initial set of coloured particles are distributed throughout the domain. This directly measures the mixing in the device, rather than relying on secondary mixing measures such as the Residence Time Distribution.

The measure is dependent on the initial set of particles that are chosen. This is important, as it is unlikely that the mixing is homogenous over the entire flow. Consider a set of particles coloured so that the domain is divided into two separate colours. The calculated mixing measure will be dependant on the rate of mixing across the interface between the two colours. In Robinson and Cleary (2010) it was shown that it is beneficial to use knowledge of the manifold geometries in the mixer in order to choose a colouring procedure which can best highlight isolated regions with poor mixing. If the initial set of particles is located within such region, then the mixing measure will give a worst-case mixing rate for the entire mixer. This is preferable to using a global measure that does not consider the inhomogeneous nature of the flow field and will therefore under-represent the effect of small isolated regions on the long-term mixing.

$M(\mathbf{x})$  is calculated at each point  $\mathbf{x}$  in the domain, and the length scale  $L$  defines a spherical region around each point with a radius of  $L$ . All the particles within this sphere contribute to the calculation of the amount of mixing at that point  $\mathbf{x}$ .

The mixing measure  $M(\mathbf{x})$  is then defined as:

$$M(\mathbf{x}) = \frac{\mathbf{s}_L(\mathbf{x}) \cdot \mathbf{s}_g - M_{\min}}{M_{\min}} \quad (9)$$

where  $\mathbf{s}_L(\mathbf{x})$  is a vector of the ratios of different coloured particles in each spherical region. Each component of the vector represents a different colour, and the length of the vector is the total number of colours  $C$ . The global ratio  $\mathbf{s}_g$  is simply  $\mathbf{s}_L(\mathbf{x})$  evaluated over the entire flow domain ( $\mathbf{s}_g$  is therefore independent of  $\mathbf{x}$ ) and  $M_{\min}$  is the minimum possible value of  $\mathbf{s}_L(\mathbf{x}) \cdot \mathbf{s}_g$ . These are defined as:

$$\begin{aligned} \mathbf{s}_L(\mathbf{x}) &= \frac{1}{\sqrt{\sum_{i=1}^C \left(\frac{n_i(\mathbf{x})}{N_i}\right)^2}} \left( \frac{n_1(\mathbf{x})}{N_1}, \frac{n_2(\mathbf{x})}{N_2}, \dots, \frac{n_C(\mathbf{x})}{N_C} \right) \\ \mathbf{s}_g &= \frac{1}{\sqrt{C}} (1, 1, \dots, 1) \\ M_{\min} &= \frac{1}{\sqrt{C}} \end{aligned} \quad (10)$$

where  $n_i(\mathbf{x})$  is the number of particles within radius  $L$  of  $\mathbf{x}$  with colour  $i$ , and  $N_i$  is the total number of particles in the simulation with colour  $i$ .

## 4 Mixing using a Single Helical Ribbon (SHR)

This section describes the flow around the SHR impellor and explores its mixing characteristics by examining its hyperbolic LCSs. Since the flow is steady within the rotating reference frame of the impellor, we can take the average of the velocity field in this frame in order to show the steady state flow pattern. Figure 4 shows the steady state velocity field for the SHR along the  $x = 0$  and  $y = 0$  plane, averaged over 55 samples of the velocity field from  $t = 7.25$  to  $10.0$  s.

The bulk motion of the fluid is controlled by a circulation cell on either side of the impellor rotation axis. They are generated by the rotation of the impellor, which

pushes the fluid near the outer boundary of the tank (i.e. near the helical ribbon) downward. Due to the presence of the bottom boundary of the tank, this gives rise to a circulation cell that moves the fluid downward and then back upward near the centre shaft of the impellor.

Superimposed on this container wide recirculatory flow is a smaller helical circulation located next to the impellor blade. This can be seen near the labels 'A' in Figure 4, where the velocity arrows form a circulating flow that occurs near the inner edge of the impellor helical ribbon. This flow pattern extends along the inner edge of the ribbon, forming a helical circulation cell that moves with the impellor. Figure 5 shows the transport and mixing of a volume of fluid initially located in the bottom quarter of the SHR mixer. Only the surface of the volume is shown and it is coloured with an initial checkerboard pattern in order to allow the deformation of the fluid volume to be visually tracked. The shape of the coloured volume is barely changed at 1 s. At 6 s, the volume has deformed significantly with the bulk of the fluid being drawn up through the centre of the mixer. The originally flat top surface of the volume has been stretched vertically and twisted around the central shaft. This forms two leading protuberances, labelled A and B in the figure, that are wrapped around the central shaft and eventually envelope the shaft and the spokes supporting the ribbon blade. At 11 s, the leading protuberance of the fluid volume has reached the top of the mixer and has begun spreading radially outward from the contact location.

This evolution continues and at 16 s the large volume of fluid being drawn up the centre and travelling along the top wall of the mixer shell has now reached the outside of the tank and is now being drawn downwards. Note also the formation of downward facing "ridge" of fluid that stretches out behind the supporting strut (label C and D). This indicates that these struts are also contributing to the mixing by elongating the fluid flowing around them and folding it around the central shaft. The bottom surfaces of the coloured volume is becoming ragged and fragmented with many separated droplets indicating the progression of the fine scale mixing in this region.

The LCSs of the flow can show the specific location and structure of the mixing processes that have deformed the fluid volume as shown in Figure 5. The repelling and attracting manifolds are given by the maxima ridges in the FTLE field. Figure 6 shows slices of the forward and backwards time FTLE fields on the  $x = 0$  and  $y = 0$

planes for  $T = \pm 6.25$  s (approximately one period of the rotating impellor). The red/orange bands of maximum forward time FTLE show the repelling manifolds, which promote stretching in the flow. Consider the pair of ridges near label A in the figure. They show the location of a pair of repelling manifolds that pull adjacent fluid volumes onto very different trajectories. Fluid located above the pair of manifolds travels upward in the mixer and is folded around the blade of the impellor. The fluid volume below the manifold pair is pushed by the downward motion of the impellor. Fluid between the manifolds moves tangentially to the other volumes, following a path between them. This fluid is stretched out into a progressively more elongated volume with each end moving along the bounding manifolds. The effect of these manifolds can be seen in Figure 5 with the sharp ridge of fluid that forms behind the protuberances at labels A and B.

The red regions in the backwards time FTLE field (right panel of Figure 6) indicate the locations of the attracting manifolds. These manifolds show the direction along which individual fluid volumes are being stretched out in the flow. Consider the ridge near label B in the figure. This shows an attracting manifold that intersects the same three fluid volumes mentioned in the earlier discussion of the repelling manifold. The fluid is being drawn upward near the centre of the mixer, and this attracting manifold and the one on the opposite side of the shaft show the path traced out by the movement of the two protuberances seen in Figure 5. The attracting manifolds show where the fluid volumes are being elongated more strongly than the surrounding fluid, and hence the protuberances are moving upward at a greater rate than the rest of the fluid volume shown in this figure.

The attracting manifolds that start from the ribbon near the bottom of the mixer show where the fluid is being drawn downward and towards the top of the ribbon blade as it moves towards the bottom boundary. This can also be seen in the last two frames of Figure 5, where the fluid near the bottom of the tank is being elongated towards the ribbon blade and then broken up into individual droplets by the high stretching zone at the bottom of the mixer.

The common feature in both the forwards and backwards FTLE field is the thin layer of red that can be seen along the outer tank wall. This is due to the high shear zone

near the no-slip boundary and is not considered to be either an attracting or repelling LCS.

Using the automatic ridge detection algorithm described in Section 3.2, the attracting and repelling manifolds of the SHR mixer have been extracted from the FTLE fields and are displayed in Figure 7. The manifolds are coloured by the local strength  $S$ , which is defined in Section 3.2 as the local curvature of the FTLE field. Blue colours indicate a high curvature and a sharply defined ridge in the FTLE field, while red colours indicate a wider ridge. Whereas Figure 6 showed only a cross-section of the manifolds, Figure 7 allows visualisation of the entire manifold structure, showing a more complete picture of the mixing. The left plot shows the repelling manifolds. The most obvious feature shown here are the two manifold surfaces emerging from the helical blade near the top of the figure (see label 'A' in the figure). These correspond with the manifold cross-section near label 'A' in Figure 6. This double manifold structure forms a continuous surface around the main axis of the mixer. It divides the fluid into three volumes that either move upwards, downwards, or are trapped between the two manifold surfaces.

The other main repelling manifold structure shown in Figure 7a is in the bottom half of the figure. The fluid located above this surface is transported inward and upward along the central axis of the mixer, whereas the fluid below this surface is moved downward to the bottom of the tank by the motion of the blade.

The plot in Figure 7b shows the attracting manifolds, which show how (along which paths) these volumes are stretched by the flow. Since the attracting manifold surfaces are surfaces of maximum FTLE, fluid located near these manifolds is being stretched out more quickly than the surrounding fluid. This means that any given fluid volume transported by the flow will begin to show features corresponding to the attracting manifold geometry.

Consider the protuberances discussed earlier and shown in Figure 5, label 'A'. The upward movement of this protuberance is due to the fluid being stretched out along the attracting manifold surface located near label 'B' in Figure 7. Similarly, the downward moving ridges of fluid located at labels 'C' and 'D' in Figure 5 are being stretch out along the attracting manifold surface near 'C' and 'D' in Figure 7.

Examined separately, the attracting and repelling manifolds give useful information on the transport patterns present in the mixer and how fluid volumes are separated, stretched and folded around the domain. Together, the intersection of the manifolds gives further insight into the mixing regions and, most importantly, where fluid transport is blocked in the flow.

Figure 8 shows the intersection of the attracting and repelling manifolds. These intersections are shown by lines that are coloured by the angle of intersection. Anywhere that the angle of intersection is less than some threshold (taken here as 45 degrees) and the manifold surfaces are closer than  $2\Delta p$ , then the manifolds are determined to be close to co-incident and therefore a barrier to mixing. These barrier surfaces are shown in the figure also coloured by the relative angle between the surfaces. The most prominent feature of Figure 8 is a quartet of intersection lines, with intersection angles close to 90 degrees, that are located at a quarter and three-quarters of the height of the tank. These are periodic orbits of the flow field that encircle the axis of the mixer, although the intersection lines tend to break up near the supporting struts of the ribbon, preventing the full description of the orbit. The lines show the location of the primary mixing regions of the SHR mixer. These regions are unchanging in time and rotate along with the motion of the impellor.

To illustrate the mixing process within these regions, Figure 9 depicts the stretching and division of a spherical volume of fluid that initially surrounds the intersection of two sets of manifolds (a set comprises one attracting and one repelling manifold). Both the attracting and repelling manifolds are shown in the image sequence, coloured blue and red respectively. Instead of visualising the manifolds over the entire domain, only the relevant subsection of the domain is shown for clarity. In frame a), the SPH particles within the spherical volume are surrounding the four curves formed by the intersection of the two sets of manifolds. The particles are coloured with an arbitrary pattern in order to visually track them between frames. In frame b), the sphere is being stretched out and upwards along the blue attracting manifold. Those particles that were located above the two red repelling manifolds are moving upward and away from these manifolds, and the particles located below the repelling manifolds are moving downward. In the frame c) the SPH particles has been divided into two sets: those particles that were above the red manifold pair and those that were

below. There is also a third set of particles that are not shown in frame c) because they have moved around the mixer and out of the narrow region that is being visualised. These particles are located in between the two red repelling manifolds and are shown in frame d). They are pulled along by the passage of the supporting strut and are being wrapped around the centre of the mixer. The particles cannot cross the repelling manifolds and are moving away from both of these surfaces, so over time they are elongated into a thin slice of fluid that wraps itself around the mixer behind the cross-struts. This highlights the contribution of the cross-struts whose inclusion is for the purposes of physically supporting the ribbon blade but which contribute to the mixing. The process shown in Figure 9 is the primary mixing mechanism for the Helical Ribbon mixer. A similar flow occurs around the manifold intersection lines in the lower half of the mixer.

Returning to the previous figure, Figure 8 also shows where the manifolds (which appear as blue shaded surfaces) are close to co-planar. These are locations where mixing is poor because fluid cannot cross these surfaces. They appear as blue shaded surfaces. Visualising these primary barriers to transport within the mixer allows us to understand which regions are not contributing to mixing. For the SHR, the primary transport barriers exist between the impellor ribbon and the central shaft near the top half (label 'A') and middle ('B') of the mixer (the surfaces at the top and bottom of the mixer are fragmentary, have less surface area and do not contribute greatly to the mixing). The flow near these barriers consists of a strong upward movement of fluid and this creates the protuberances that have already been described in Figure 5. While the strong vertical flow causes rapid stretching of fluid elements in the vertical direction, there is little or no movement of fluid in the radial direction, leading to these barriers to mixing. From the location of these barriers, it is expected that the slowest mixing will occur between the inner and outer regions of the mixer. This will be investigated further, using a quantitative mixing measure, in Section 7.

## **5 Mixing using a Double Helical Ribbon (DHR)**

The DHR impeller is similar to the SHR except that another helical ribbon has been added 180 degrees out of phase with the first. This does not change the basic structure of the flow, but merely superimposes the effects of the new ribbon onto the flow field.

Figure 10 shows the radial velocity field on the  $x = 0$  and  $y = 0$  planes. The primary flow still moves down the outer annulus of the mixer and up through the central region around the shaft. The use of two blades significantly increases the strength and speed of this recirculatory flow which is now fairly uniform with height. As occurred for the SHR, each ribbon has a local helical circulation cell located just inside the ribbon blade. The increased relative strength of the overall recirculation means that these local flow structures now appear more as perturbations.

To compare the fluid transport between the SHR and the DHR designs, a time sequence showing the evolution of an initial sphere of fluid is shown in Figure 11. The left column shows the SHR while the centre column shows the DHR. The average fluid velocity in the DHR is significantly higher than the SHR, which means that the fluid sphere is pulled up through the centre of the mixer at a significantly faster rate than for the SHR. This, coupled with the additional mixing ribbon (and therefore double the number of circulation cells) causes the sphere to be stretched out and deformed much more quickly, leading to what appears to be a higher mixing rate in the DHR.

The mixing processes in the DHR and the SHR appear similar in structure; except that the additional ribbon in the DHR results in double the number of mixing regions in the flow. For example, compare frame 2 for the DHR and frame 3 for the SHR. The fluid sphere has reached a comparable point in the flow, which allows us to compare the deformation of the sphere while accounting for the increased velocity in the DHR. While the spheres in both mixers have been stretched out in a similar fashion up to this point, the DHR sphere is being more quickly broken up by the additional supporting struts. By the end of the sequence, the fluid volume in the DHR has reached the top of the mixer and is beginning to move down the outside of the tank. In contrast, the SHR volume is still in the core of the tank and moving upward in a coherent form.

While the time sequences shown in Figure 11 are useful to illustrate some of the short-time mixing processes, they are limited due to the fact that they only show the mixing for a specific volume of fluid and do not show or provide insight into the transport of fluid elsewhere in the mixer. They also cover a very short period of time, only one period of the mixer, which is at most a tenth of the time taken to completely

mix the given sphere of fluid with the rest of the domain. Therefore the focus of this paper is to instead use the repelling and attracting manifolds to provide a picture of the mixing processes over the entire domain, and to quantify the long term mixing rates by measuring the mixing of different regions over time (Section 7).

Figure 12 shows the repelling and attracting manifolds for the DHR. The manifold geometry around each ribbon is qualitatively similar to that of the SHR. A pair of attracting manifolds runs upwards and inwards from each ribbon, mirroring a pair of repelling manifolds that run downwards and inwards from each ribbon. These surfaces are more vertically orientated than in the SHR, and there are other specific differences due to the reduced distance between the ribbons. For example, for each pair of manifolds associated with one ribbon, the outer manifold often merges into the inner manifold of the other ribbon. However, the general structure of the manifolds remains similar.

Figure 13 shows the lines of intersection and the coincident manifolds for the DHR. Due to the extra manifolds from the new ribbon, there are an increased number of manifold intersections that are more evenly distributed throughout the mixer. This leads to more opportunities for mixing. However, as the manifolds are more vertically orientated than for the SHR, they intersect each other at lower angles of intersection, leading to a slower rate of mixing across the intersection manifold pairs (recall the explanation in Section 3). In Figure 13, this is visualised by a larger area of barrier surfaces which roughly surround a cylindrical volume around the central axis of the mixer. These barriers slow the mixing of fluid across the surface of this cylinder (between the inner and outer regions of the mixer).

In summary, the addition of a ribbon to the Helical Ribbon mixer affects the mixing in two competing ways. The extra ribbon generates double the number of circulation cells that can mix the fluid, doubling the number of repelling and attracting manifolds and their intersections. However, the vertical orientation of these manifolds means that the radial mixing is less efficient.

## **6 Mixing using a Single Helical Ribbon with Central Screw (CSR)**

The CSR mixer is identical to the SHR, except for the addition of a screw impeller blade that encircles the central shaft of the mixer. The screw imparts a small downward velocity to the nearby fluid (see Figure 14), which acts against the bulk annular recirculation that was present in the SHR. The helical recirculation cells are qualitatively similar to the SHR, but appear slightly more dominant due to the reduction in the bulk annular recirculation. From the velocity field it is very difficult to judge the effect of this additional screw on the mixing process. In contrast, the manifold structure for the CSR can provide useful insight that would be difficult to obtain otherwise.

Figure 15 shows the repelling and attracting manifolds for the CSR. Those generated by the original helical ribbon still dominate the domain, and are indistinguishable to those seen in the SHR. However, the screw blade generates its own set of manifolds that run down the middle of the mixer, close to the screw. These are inside the manifold created by the ribbons and are not clearly visible in Figure 15. These inner manifolds are shown more clearly in Figure 16. It shows a comparison of the manifold structure along the  $x = 0$  plane for the SHR and CSR mixers. The repelling manifolds are drawn as red while the attracting ones are blue. The white solid areas are the mixer geometry. The left hand frame shows the manifolds for the SHR and is a cross-section of the manifold structure shown in Figure 7. On the right are the manifolds for the CSR. Most of the manifold structure in the outer half of the mixer is similar for both mixers, but in the CSR there is a new set of manifolds near the central shaft that closely follow the screw geometry. Considering just the additional manifolds, both the repelling and attracting ones are orientated close to vertical and are close to co-planar for a significant proportion of the tank height. This indicates that the flow generated by the screw is causing the fluid immediately surrounding the central shaft of the mixer to be isolated and slow to mix with the rest of the domain. Mixing of fluid initially close to the shaft will be accomplished quickly but the mixing of this fluid with the large bulk of the rest of the mixer will be therefore be quite slow.

This new mixing flow around the central screw is not entirely separate from the mixing in the outer regions. Near the label 'A', a pair of repelling manifolds from the outer annular region is linked up with the manifolds surrounding the screw. This is generated by the motion of the central struts, which extend from the central shaft to the outer impellor ribbon.

Figure 17 shows the lines of intersection and coincident manifolds for the CSR. The lines of intersection that are associated with the outer helical ribbon are similar to the SHR, except that the angle of intersection in some regions is slightly lower for the CSR. However, the similarity of the manifold structure seen near the original helical ribbon indicates that the mixing near the ribbon is similar for both mixers. The main difference between the SHR and the CSR occurs near the screw impeller, where the manifold structure shows that the addition of the central screw creates numerous barriers to transport between the region close to the central shaft and the outer parts of the mixer. The effects of this barrier can be also seen in the deformation of the fluid sphere shown in Figure 11 (right column). The sphere is seen to closely hug the central screw as it is pulled up along the centre of the mixer (The frames at  $t = 8.5$  s shows this most clearly). The overall transport of the fluid volume upwards is also slower than the SHR, which is consistent with the weakening of the bulk flow in the velocity field shown in Figure 14.

In summary, the addition of a central screw does not provide any noticeable improvements to the Helical Ribbon mixer. In fact, the screw reduces the overall rate of bulk recirculation and acts to isolate a central core region of the fluid.

## **7 Comparative mixing rates for the different impellers**

The previous three sections discussed the qualitative differences in the mixing structure of the flow for the three different mixer geometries. In order to quantitatively investigate these behaviours and to explicitly compare the mixing rates for the three impellers, we have calculated the mixing measure  $M(\mathbf{x})$  defined in Section 4.3 to all three simulations. This mixing measure  $M(\mathbf{x})$  can be used to evaluate the degree of mixing between different volumes of fluid defined by classifying the fluid according to its initial location. Three different pairs of volumes were studied:

1. Vertical partitioning into two volumes on either side of the  $x = 0$  plane
2. Annular partitioning with an inner cylindrical volume of radius 40 mm and an annular outer region.
3. Annular partitioning with the inner cylinder having radius 16 mm

The first pair was chosen to show the mixing rate between the two vertical halves of the mixer. The second was designed to show the mixing rate across the set of (approximately) cylindrical manifolds around the DHR (see Figure 13). The third shows the mixing rate between the region immediately surrounding the central screw in the CSR, and the remainder of the domain. A characteristic length scale of  $L = 6$  mm (the minimum resolution for the simulation) was used for the mixing measure.

Figures 18-20 shows the plot of average  $M(\mathbf{x})$  versus time,  $\overline{M}(t)$ , for all three mixers and the three different partitioning schemes. At the start of the simulation the two fluid volumes are separate and  $\overline{M}$  is close to zero (the only non-zero contribution to  $\overline{M}$  occurs around the interface between the volumes). As time progresses the volumes are stretched and folded around each other, increasing their interface area and therefore the value of  $\overline{M}$ . After a certain time the rate of increase levels off near  $\overline{M} = 1$  as the volumes become completely mixed. Note that  $\overline{M}$  will not quite reach unity because of the finite numerical resolution and the random fluctuations in the particle distributions which occur over time.

In Figure 18, for the vertical partitioning of the volumes, it can be seen that the DHR has the fastest rate of mixing reaching a value of  $\overline{M} = 0.9$  after approximately 65 s, compared to 94 s for the CSR and 97 s for the SHR. The difference in the rate of the mixing is relatively modest for the different impellers. The DHR certainly does not mix at double the rate just because it has double the ribbons of the SHR.

The differences in mixing rates between the mixers are proportional to the energy transferred to the fluid by the rotation of the impellor. To illustrate this, Figure 18 (insert) scales the time axis by the (constant) power input for each of the impellers, therefore showing the mixing measure versus the energy supplied. In this case, all the three plots collapse on top of each other, indicating that the efficiency of mixing

between the two halves of the mixer (in terms of the energy used) is the same for all the mixers. The CSR supplies energy slightly faster and mixes slightly faster, while the DHR supplies energy moderately faster and mixes commensurably faster.

Given the similar mixing rates for the vertical slices, this partitioning is not useful to separate the mixers in terms of their mixing quality. The geometry of the manifolds has shown that the limiting mixing rate for all three geometries occurs between the inner and outer regions of the tank, and therefore the next few mixing plots will examine the mixing rate between these regions. This highlights the contribution of the LCSs to the measurement of mixing and the quantitative comparison of the three geometries. Any mixing measure needs to take into account that fact that the mixing is unlikely to be homogenous over the entire domain, and there might be many different timescales of mixing. The geometry of the LCSs can be used to identify the main barriers to mixing in order to target the mixing measure to these areas and directly compare the worst-case mixing rates for the different impellers.

Figure 19 shows the mixing between the second pair of volumes, with the inner cylindrical region of radius 40 mm and the outer annular one. For both the SHR and the CSR, the mixing rate is slower than for the vertical partitioning. The manifold intersections for the SHR and the CSR (Figures 8 and 17) showed that the main barriers to mixing acted to slow the mixing in the radial direction. This is consistent with these results, which also show that the radial mixing rate (across the cylinder of radius 40 mm) is reduced for these geometries. The rate of radial mixing for the DHR is improved moderately in comparison the other two impellers. The qualitative analysis of the manifold structure and flow patterns from the DHR concluded that there were two competing effects of adding the additional ribbon. The new ribbon generated twice the number of mixing regions and their associated manifold structures, but the new geometry of these manifolds showed a reduction of the mixing efficiency between the inner and outer regions of the tank (i.e. the same annular partitioning that is used for the calculation of this figure). Given the increased rate of radial mixing seen in Figure 19, it can be concluded that the effect of increasing the number of mixing regions is the stronger of the two competing effects, leading to more efficient mixing for the DHR compared to the SHR.

The mixing measure versus time for the third pair of volumes is shown in Figure 20. The inner cylinder in this case is much thinner than the second pair, and only covers the local region around the central screw in the CSR. This plot shows that the mixing rate across this inner cylinder has decreased for the CSR, in comparison with the other two impellers. This demonstrates that the vertically aligned coincident manifolds are restricting the mixing of this fluid with the rest of the domain. So for mixing of fluid close to the shaft, the inclusion of the inner screw blade is a retrograde step since it leads to the trapping of this fluid against the shaft.

While the CSR impellor exhibits the largest reduction in mixing rate, the mixing rate for all three impellers is lower for this fluid partitioning than for the annular partitioning with a larger radius. This is not due to any particular manifold structure, but is simply a result of the lower surface area between these volumes, which restricts the amount of fluid that can be transferred across the interface.

## **8 Assessing the contribution of the ribbon and its cross bar supports**

In the earlier manifold analysis we saw that both the ribbon blade and its cross bar supports generated manifold structures and therefore both contribute to the mixing process. Using simulation, we can perform an investigation that cannot be performed with any experiment, that is, we can independently investigate the contributions of the mixing ribbon elements and the cross-bar structural elements whose intended purpose in the design is to physically support the ribbon blade. Two additional impellor geometries were simulated. One impellor consisted only of the helical ribbon, with no supporting struts (SHR-R). The other consisted of just the horizontal cross bar struts, with no ribbon blades (SHR-A).

Figure 21 shows a time sequence of the transport and mixing of an initial sphere of fluid, similar to what was shown for the other three impellor geometries in Figure 11. For the ribbon-only impellor, the transport and mixing of the sphere in the vertical direction is very similar to the SHR. The ribbon provides the overall fluid circulation rising upward through the central region of mixer and then down in the outside annular region. It also generates circulation cells near the inside edge of the ribbon. Comparing the time sequence in Figure 21 to that of the SHR in Figure 11, the main

difference between the two fluid flows is the reduced stretching around the main axis of the SHR-R and much less breakup of the surface of the volume. In contrast, as the struts in the SHR sweep around this shaft, they drag a reasonable amount of fluid from the sphere along with them, contributing to the mixing in the direction of rotation.

The strut-only impellor geometry (SHR-A) shown in Figure 21 shows how the struts transport fluid in the direction of rotation. Without the ribbon fluid motion is predominantly horizontal with fluid dragged circumferentially around the mixer but with little axial motion. The initially spherical volume in this time sequence does not move at all in vertical direction. The struts cut through the fluid entrain nearby fluid which is dragged around the central shaft of the mixer. There is significant and rapid stretching of the fluid volume, but there is not folding component (which is always required for good mixing). There is also good dispersion of small droplets at the periphery of the representative volume in the plane of the struts. The struts clearly have a very strong local mixing effect on the fluid but their influence rapidly declines with increasing distance from the plane of the struts.

These time sequences show that the fluid flow generated by both the struts and the helical ribbon are distinct and interact only weakly. The rotation of the ribbon generates the large and small cells that circulate the fluid in the vertical direction, while the struts strongly mix fluid that is close to their rotation planes in the circumferential direction.

In order to quantify the contribution of these actions to the mixing we will again use the average mixing measure  $\bar{M}$ . Figure 22 shows  $\bar{M}$  versus time for the vertical partitioning used in the previous section, and compares the results for the SPH, SHR-R and SHR-A mixers. The mixing rate for the SHR-R and SHR-A mixers are almost equal for this partitioning. While the SHR-A does not have the global circulation present in the SHR-R, it is highly effective at mixing in the circumferential direction and therefore is well suited for this particular partitioning. Without the supporting struts, the mixing rate for the SHR-R is significantly reduced from that of the SHR. Therefore, for the helical ribbon mixer, the struts provide a significant contribution, equal to the ribbon itself, to the mixing around the axis of rotation.

Figure 23 shows  $\bar{M}$  versus time between the second set of volumes: the inner cylindrical region of radius 40 mm and the outer annular one. Here the SHR-A impellor has a small, constant mixing rate that is significantly lower than both the SHR and the SHR-R. The cylindrical partitioning in this case measures the radial mixing, and while the SHR-A mixer does mix fluid in the radial direction, this is slow and acts only within a narrow disc of fluid around the same height of each of the struts. This radial mixing can be seen in the evolution of the fluid sphere in Figure 21, which shows a narrow, horizontal disc of fluid being stretched out by the struts. Since this is a local process in a relatively small area, it contributes only modestly to the global mixing rate. This is also seen in the radial mixing measure for the SHR-R, which is similar in form to that of the SHR but around 10% lower. This indicates that the struts make a small positive effect on the radial mixing which increases slowly over time.

## **9 Conclusion**

This paper has studied the mixing flow within three variants of the well-known helical ribbon mixer, consisting of a single helical ribbon impellor (SHR), a double helical ribbon (DHR) and a single helical ribbon combined with a central screw (CSR). The SPH method was used to solve for the fluid transport, due to its ability to handle complex, moving geometries and easy access to the complete time history of every fluid particle.

The mixing structures of the flow were visualised by extracting the hyperbolic Lagrangian Coherent Structures (LCSs) of the flow from the SPH particle data. The calculation of Finite-Time Lyapunov Exponents (FTLE) for particle methods was extended to 3D and a ridge detection method was developed to automatically extract the repelling and attracting manifolds from the FTLE fields. The methodology to identify and visualise the manifold intersections (lines for good mixing and near-coincident manifolds as barriers to mixing) was formulated, and its application to understanding the spatial structure of fluid transport and was demonstrated using the three helical ribbon mixers. These combined with a quantitative mixing measure in order to provide a rigorous and flexible method for comparison of different impellor geometries.

The base SHR impellor creates a global circulation cell that moves fluid upward in the inner region of the mixer and down the outside. Smaller circulation cells near the inner edge of the ribbon generate chaotic mixing regions, which act as the primary mixing mechanism. The circulation cells create two sets of attracting and repelling manifolds which control how the fluid is transported in and around the cells. The two repelling manifolds divide the fluid into three regions that are either (a) stretched out along the attracting manifolds towards the top of bottom of the mixer or (b) pulled along by the supporting struts in the circumferential direction. The main barriers to mixing also occur near the circulation cells, while there is a strong mixing vertically and around the rotation axis, there is less radial fluid transfer between the inner and outer regions of the tank.

The addition of an extra ribbon (the DHR) doubles the number of mixing regions and therefore the number of manifold sets. The geometry of the new manifolds is similar to the SHR, but both sets of manifolds are more vertically aligned in this mixer geometry, strengthening the barrier to transport that exists between the inner and outer regions of the mixer. While there is now double the number of mixing regions in the flow, the efficiency of the mixing for each region is reduced and the overall mixing rate is only moderately increased rather than doubled.

The addition of a central screw to the SHR impellor does not significantly change the mixing structures or the manifolds near the helical ribbon. However, the manifold structures created around the central screw are close to coincident, slowing the mixing of fluid immediately surrounding the screw with the remainder of the domain. The addition of the central screw is therefore counter-productive as it reduces the homogeneity of the mixing.

The influence of the supporting struts on the mixing (difficult to perform experimentally) was studied using SPH simulations of a single helical ribbon with no struts (SHR-R), and an impellor with the struts included but no helical ribbon (SHR-A). As the struts rotate, they cut into and entrain the fluid, stretching it around the axis of rotation. This circumferential mixing from the struts is equal in strength to that provided by the ribbon itself. However, the struts only provide a small increment to the radial mixing and their influence is restricted narrow discs of fluid surrounding the rotation plane of each of the struts. While the helical ribbon generates a domain

filling, chaotic flow that mixes through both stretching and folding actions, the flow around the struts is local in nature and lacks any folding actions, leading to poor global mixing in the strut-only mixer geometry. However, the two elements work well together, with the ribbon generating the global circulation that rapidly transports new unmixed fluid into the neighbourhood of the struts where it is sheared and stretched by the strong local mixing action of the struts.

This paper has shown that the mixing analysis methodology presented is effective at describing qualitatively and quantitatively the mixing within a typical three-dimensional industrial mixer, and the effect that impellor geometry has on the mixing. This data can be used to inform future impellor designs. The method is robust and flexible, and can be applied to any mixer geometry, including complex intermeshing parts and fluid free surfaces. While the mixing flow considered in the paper is steady, the methodology can equally be applied to non-steady and transient flows.

## **10 Bibliography**

- Aldridge, B. B., Haller G, Sorger P. K., Lauffenburger, D. A., (2006) Direct Lyapunov exponent analysis enables parametric study of transient signalling governing cell behaviour. *IEEE Proceedings Systems Biology*. 6(153); 425-432.
- Carreau, P. J, Patterson, I. and Yap, C. Y (1976) Mixing of viscoelastic fluids with helical-ribbon agitators. I-Mixing time and flow patterns. *The Canadian Journal of Chemical Engineering*, 54(3).
- Chavan, V. V and Ulbrecht, J. (1973) Internal circulation in vessels agitated by screw impellers. *Chem. Eng. J*, 6:213-223
- Chavan, V. V, Ford, D. E and Arumugam, M. (1975) Influence of fluid rheology on circulation, mixing and blending. *The Canadian Journal of Chemical Engineering*, 53(6).
- Cleary, P. W., Prakash, M., Ha, J., Stokes, N. and Scott, C., (2007) Smooth Particle Hydrodynamics: Status and future potential. *Progress in Computational Fluid Dynamics*. 7: 70-90.

Colagrossi A. and Landrini M., (2003) Numerical simulation of interfacial flows by smoothed particle hydrodynamics, *Journal of Computational Physics*, 191:448–75

Cummins, S.J., Silvester, T.B. and Cleary, P.W., (2012) Three-dimensional wave impact on a rigid structure using smoothed particle hydrodynamics. *International Journal for Numerical Methods in Fluids*. 68(12):1471–1496

De La Villeon, J. Bertr., F. , Tanguy, P. A., Labrie, R. , Bousquet, J. and Lebouvier, D. (1998) Numerical investigation of mixing efficiency of helical ribbons. *AIChE Journal*, 44(4).

Delaplace, G., Leuliet, J. C., Relandeau, V. (2000) Circulation and mixing times for helical ribbon impellers. Review and Experiments. *Experiments in Fluids*, 28(2):170-182

Eberly, D. Ridges in Image and Data Analysis. Kluwer, 1996

Guerin, P., Carreau, P. J., Patterson, W. I., and Paris, J. (1984) Characterization of helical impellers by circulation times. *The Canadian Journal of Chemical Engineering*, 62(3).

Haller, G., and Yuan G., (2000) Lagrangian coherent structures and mixing in two-dimensional turbulence, *Physica D: Nonlinear Phenomena*, 147(3-4): 352-370

Haller, G., (2001) Distinguished material surfaces and coherent structures in three-dimensional fluid flows, *Physica D: Nonlinear Phenomena*, 149(4):248-277

Haller, G., (2002) Lagrangian coherent structures from approximate velocity data, *Phys. Fluids A14* (2002) 1851-1861

Haralick, R., (1983) Ridges and valleys on digital images, *Computer Vision, Graphics, and Image Processing*, Volume 22, Issue 1, Pages 28-38

Khayyera, A. and Gotoha, H., (2010) On particle-based simulation of a dam break over a wet bed, *Journal of Hydraulic Research*, 48(2): 238-249

Lancaster, P., and Salkauskas, K. (1981). ‘Surfaces Generated by Moving Least Squares Methods’. *Mathematics of Computation* 37(155):141–158.

Lindeberg, T., (1996) Edge Detection and Ridge Detection with Automatic Scale Selection, *IEEE Computer Society Conference on Computer Vision and Pattern Recognition (CVPR'96)*, p. 465

Lipinski, D. and Mohseni, K. (2010), A ridge tracking algorithm and error estimate for efficient computation of Lagrangian coherent structures, *Chaos*, 20(1): 017504-017504

Liu, W. K., Jun, S. and Zhang, Y. F. (1995), Reproducing kernel particle methods. *International Journal for Numerical Methods in Fluids*, 20: 1081–1106.

Lorensen, W. E., and Cline, H. E., (1987). Marching cubes: A high resolution 3D surface construction algorithm. *SIGGRAPH Comput. Graph.* 21(4): 163-169

Metcalf, G. (2010) Applied fluid chaos: designing advection with periodically reoriented flows for micro to geophysical mixing and transport enhancement. In *Complex physical, biophysical, and econophysical systems* (eds R. Dewar & F. Detering). Lecture Notes in Complex Systems, pp. 189-242. Singapore: World Scientific

Metcalf, G., Rudman, M., Brydon, A., Graham, L. & Hamilton, R. (2006) Composing chaos: an experimental and numerical study of an open duct mixing flow. *AIChE J.* 52, 9-28

Ottino, J., *The kinematics of mixing: stretching, chaos and transport*: Cambridge University Press; 1989.

Patterson, W. I., Carreau, P. J., and Yap, C. Y., (1979) Mixing with helical ribbon agitators: Part II. Newtonian Fluids. *AIChE Journal*, 25(3):508-516.

Pierrehumbert, R. T, Yang, H. (1993) Global chaotic mixing on isentropic surfaces. *Journal of the Atmospheric Sciences*; 15(50); 2462-2480.

Robinson, M., Cleary P. W., Monaghan J. J., (2008) Analysis of mixing in a Twin-Cam mixer. *AIChE Journal*; 54: 1987-1998.

Robinson, M., Cleary P. W.,(2010) The Influence of Cam Geometry and Operating Conditions on Chaotic Mixing of Viscous Fluids in a Twin Cam Mixer. *AIChE Journal*; 57: 581–598

Sadlo F, Peikert R. (2009) Visualizing Lagrangian Coherent Structures and Comparison to Vector Field Topology. *Topology-Based Methods in Visualization II*; 15-29.

Shadden, S. C., Lekien, F., Marsden J. E.. (2005) Definition and properties of Lagrangian coherent structures from finite-time Lyapunov exponents in two-dimensional aperiodic flows. *Physica D Nonlinear Phenomena*. 212: 271–304.

Tanguy, P. A., Lacroix, R., Bertrand,, F., Choplin, L. and de la Fuente, E. B. (1992) Finite element analysis of viscous mixing with a helical ribbon-screw impeller. *AIChE Journal*, 38(6):939-944.

Tanguy, P. A., Thibault, F., Brito-De La Fuente, E. , Espinosa-Solares, T. and Tecante, A. (1997) Mixing performance induced by coaxial flat blade-helical ribbon impellers rotating at different speeds. *Chemical Engineering Science*, 52(11):1733-1741

Wiggins, S., *Chaotic Transport in Dynamical Systems*. Springer-Verlag; 1992.

Zhang, M. and Batra, R. C., (2009) Symmetric Smoothed Particle Hydrodynamics (SSPH) Method and Its Applications to Elastic Problems, *Computational Mechanics*, 43, 321-340.

## 11 Figures

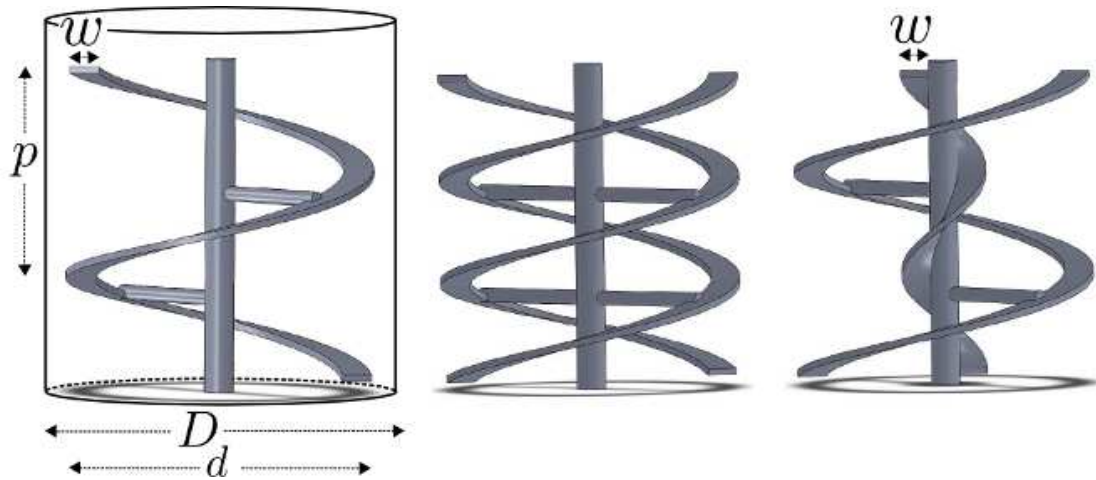


Figure 1: The three helical ribbon impellers used in this study. From left to right: The Single Helical Ribbon (SHR), the Double Helical Ribbon (DHR) and the SHR with a Central Screw (CSR). The SHR also shows the geometry of the outer tank.

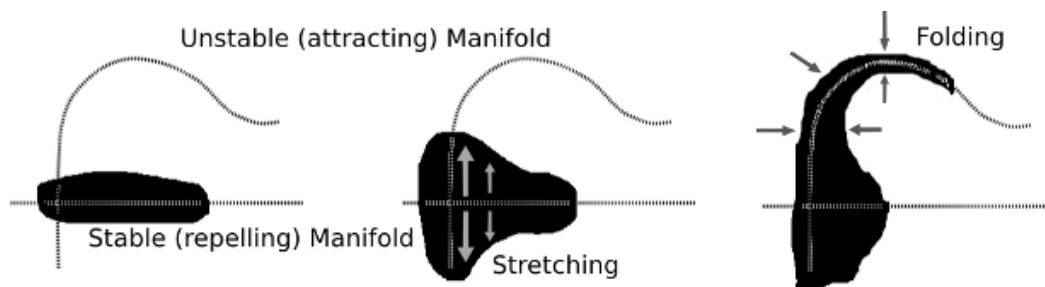


Figure 2: Diagram showing the stretching and folding of fluid regions surrounding the repelling and attracting manifolds.

Fluid flux proportional to area of lobes

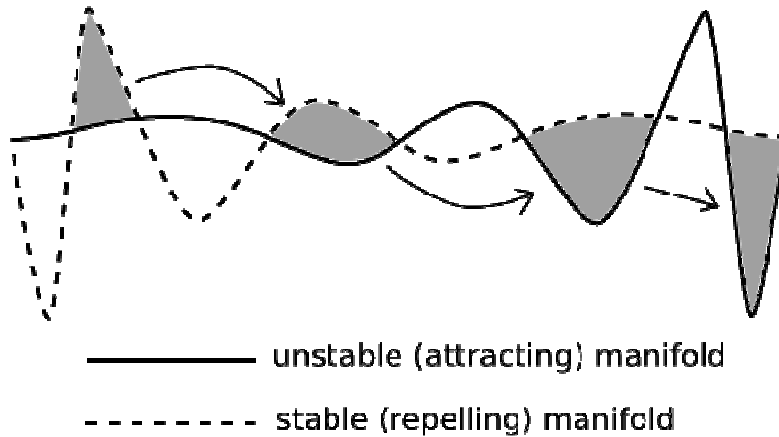


Figure 3: Diagram showing the transport of a single lobe of fluid (coloured grey) across a tangle of manifolds in a periodic flow. After each period the manifolds have returned to their original position, and the grey areas show the position of the same lobe of fluid at subsequent periods.

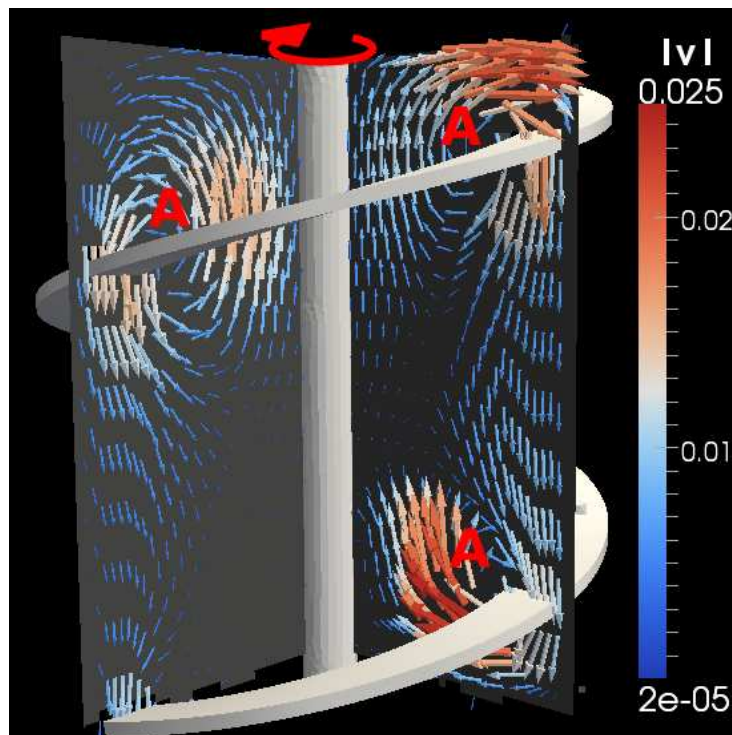


Figure 4: The three dimensional velocity field on the  $y = 0$  and  $x = 0$  planes for the SHR mixer. The arrows show the velocity components parallel to the planes and are coloured by speed and have length proportional to speed.

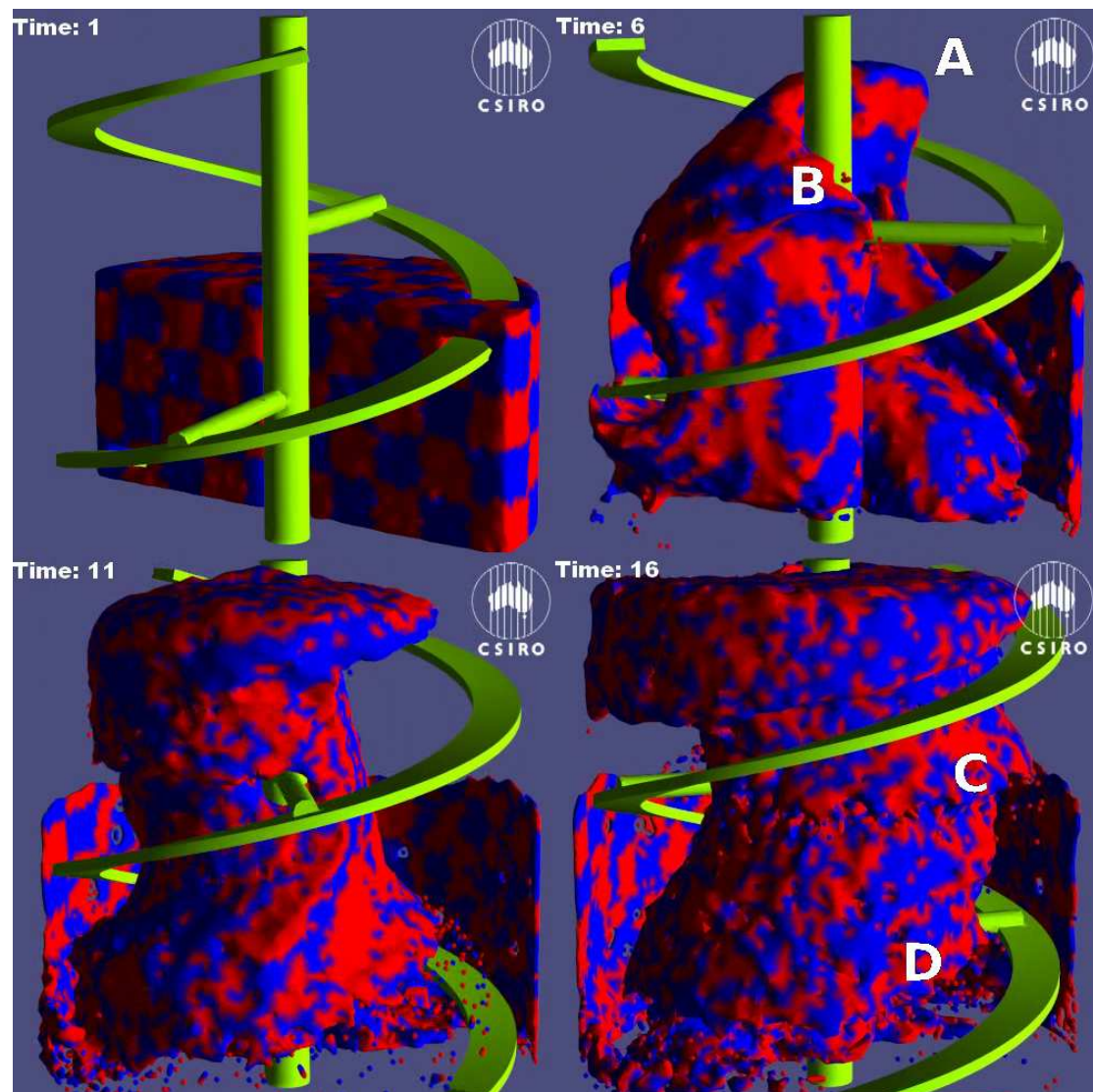


Figure 5: Transport and mixing of a representative volume of fluid initially covering a lower quarter of the SHR tank. The fluid volume is coloured by an arbitrary checkerboard pattern in order to show the movement of the fluid.

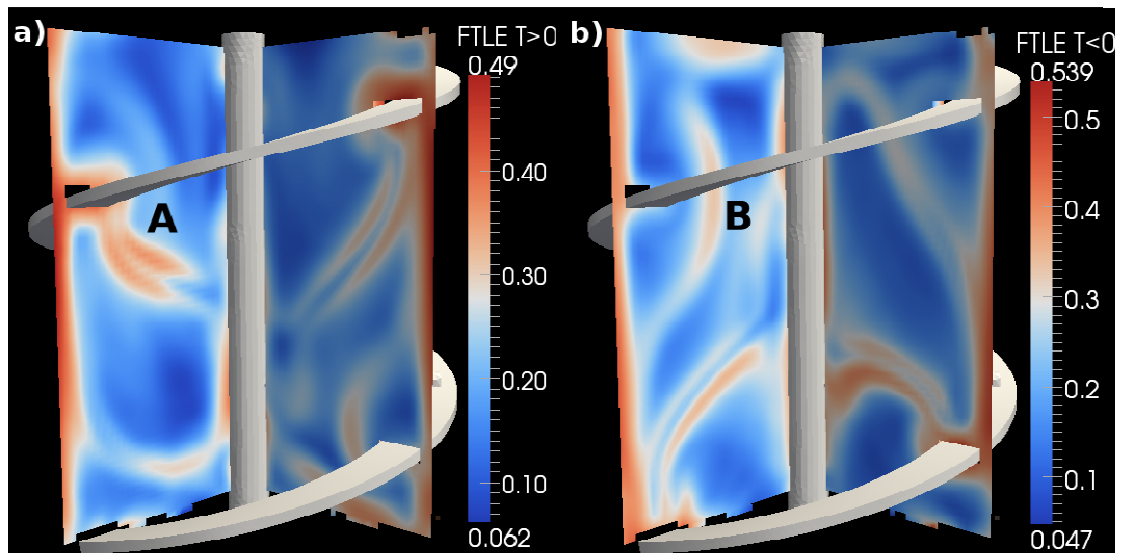


Figure 6: a) forward time ( $T > 0$ ) and b) backwards time ( $T < 0$ ) FTLE fields along the  $x = 0$  and  $y = 0$  planes. The red regions in a) show the repelling manifolds, and in b) show the attracting manifolds.

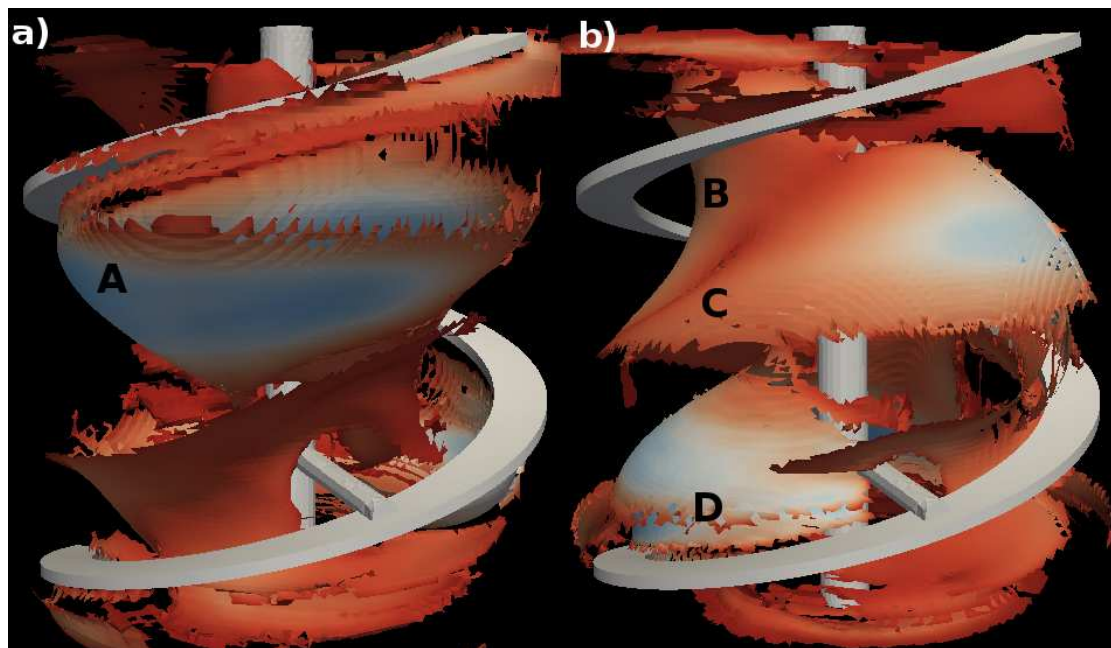


Figure 7: The LCSs for the SHR, a) repelling and, b) attracting. The manifold surfaces are coloured by the strength  $S$  of the manifold with blue indicating a strong sharp ridge in the FTLE field and red a fainter or wider ridge.

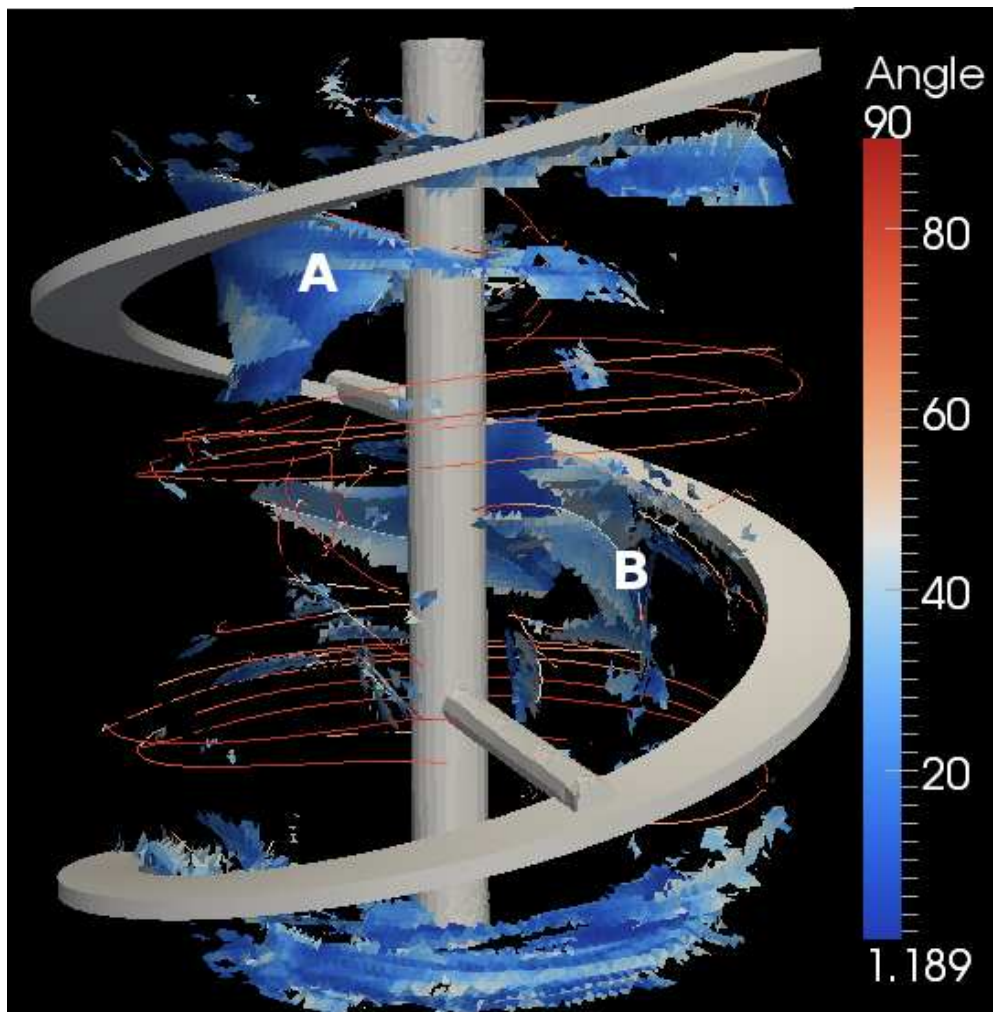


Figure 8: Manifold intersections for the SHR. Lines indicate where the repelling and attracting manifolds intersect with their colour showing their angle of intersection. The surfaces show the co-incident manifolds which act as barriers to mixing. These surfaces are also coloured by the relative angle of the manifolds.

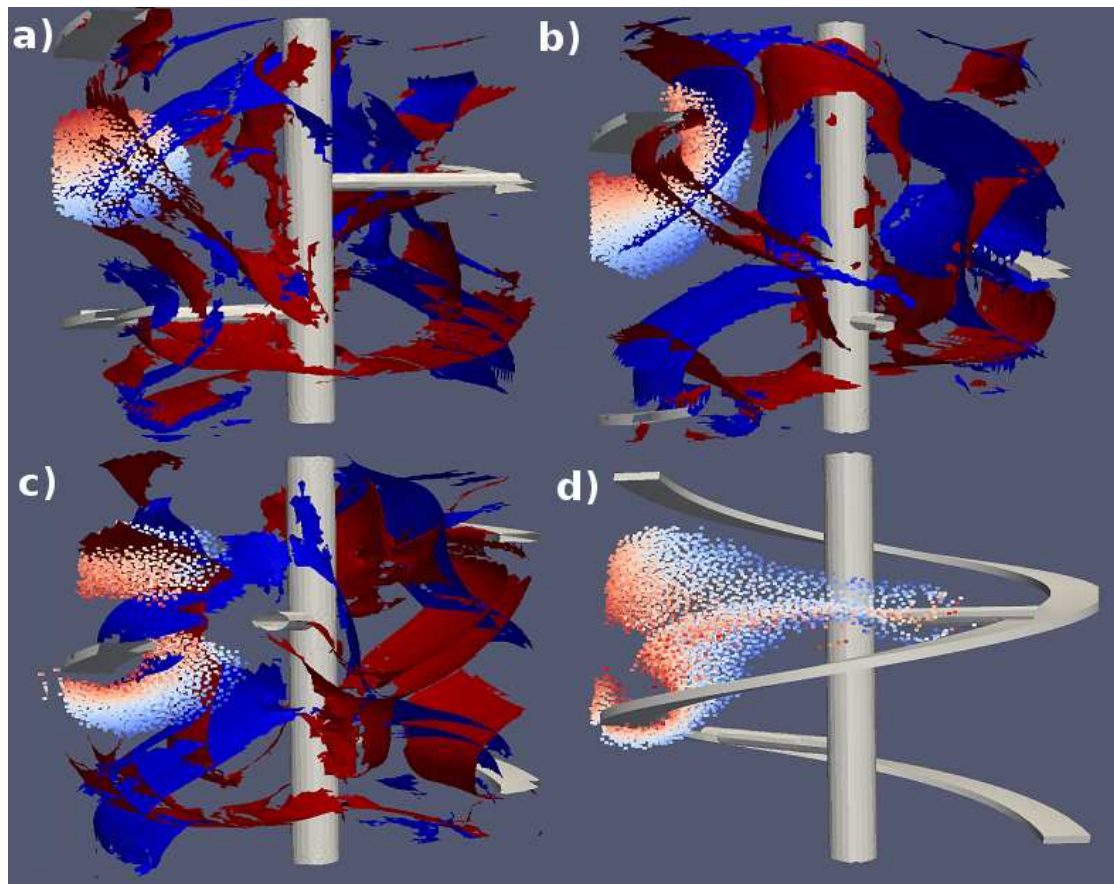


Figure 9: Time sequence showing the stretching and division of a volume of fluid (here shown as individual SPH fluid particles coloured with an arbitrary pattern) surrounding one of the manifold intersections. Attracting manifolds are coloured blue and repelling ones are coloured red.

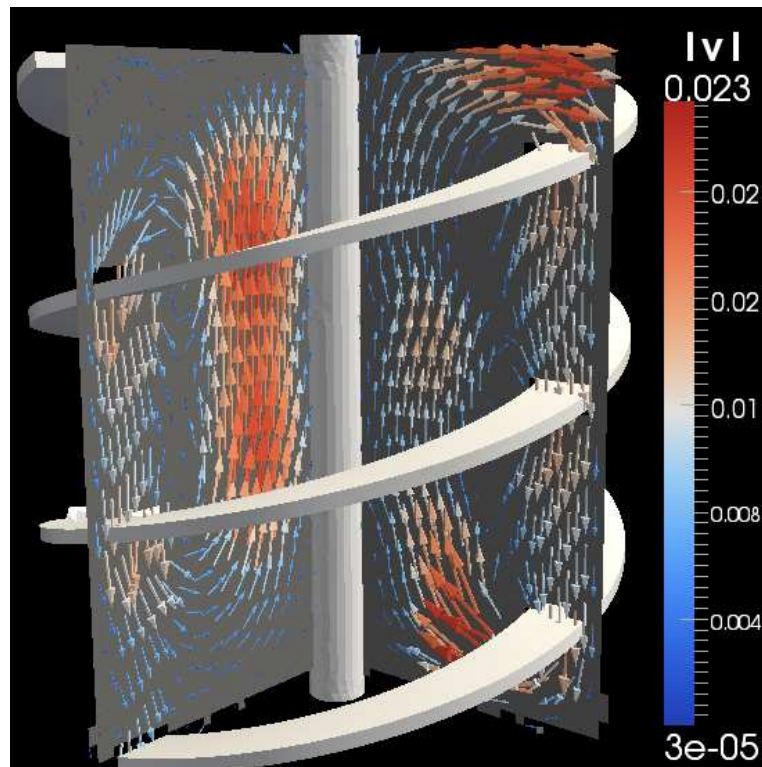


Figure 10: The three dimensional velocity field on the  $y = 0$  and  $x = 0$  planes for the DHR mixer. The arrows show the velocity components parallel to the planes and are coloured by speed and have length proportional to speed.

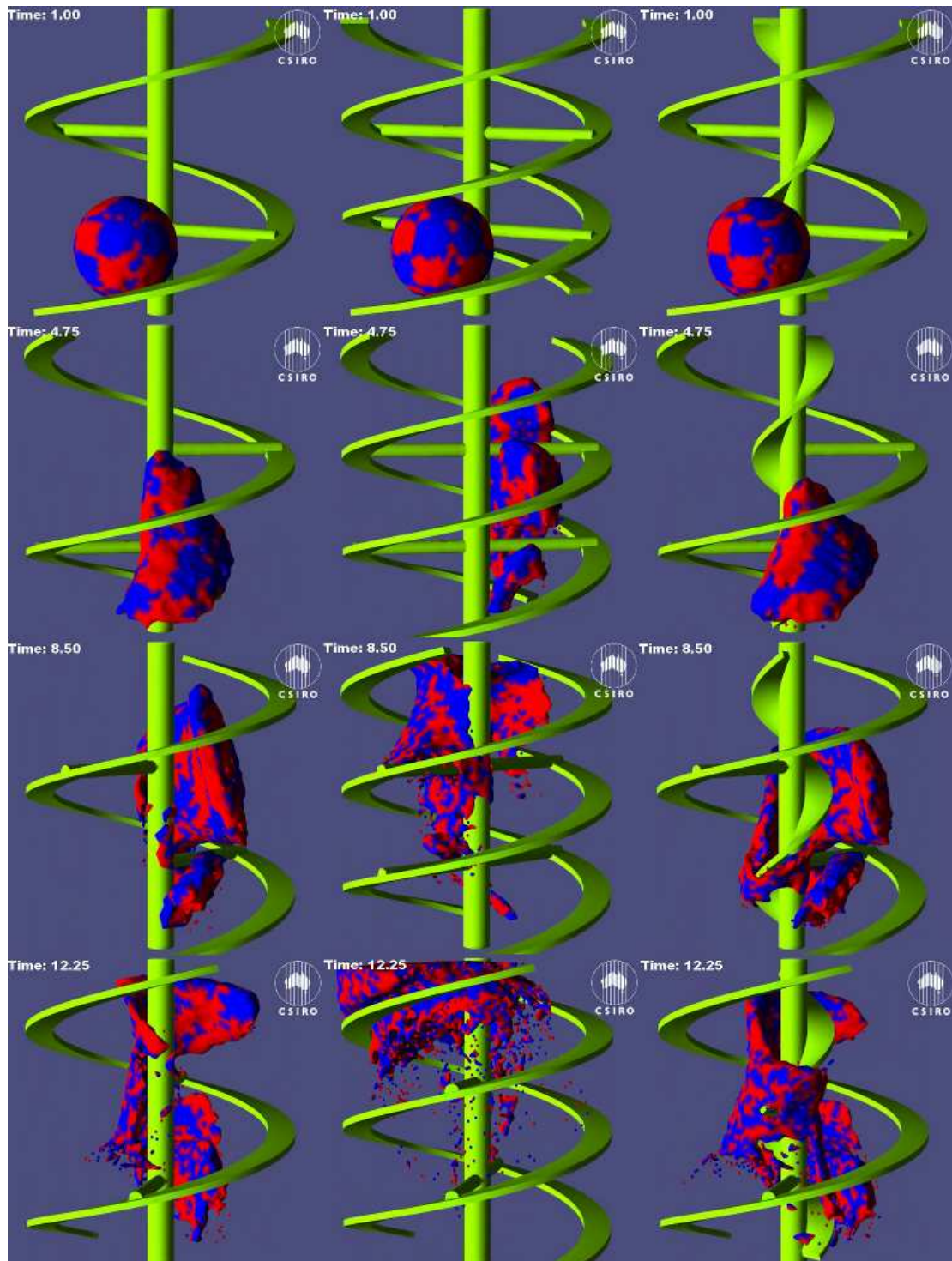


Figure 11: Time sequence showing the transport of a sphere of fluid in the SHR (left), the DHR (centre) and the CSR (right). Only the surface of the fluid volume coloured with an arbitrary pattern is shown.

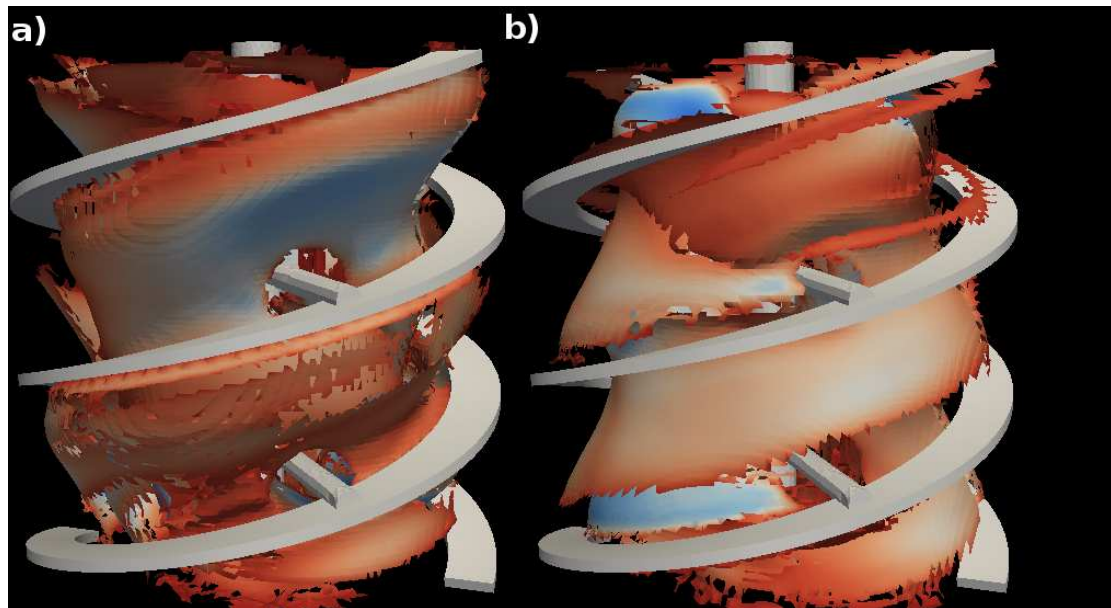


Figure 12: The LCSs for the DHR, a) repelling and, b) attracting. The manifold surfaces are coloured by the strength  $S$  of the manifold with blue indicating a strong sharp ridge in the FTLE field and red a fainter or wider ridge.

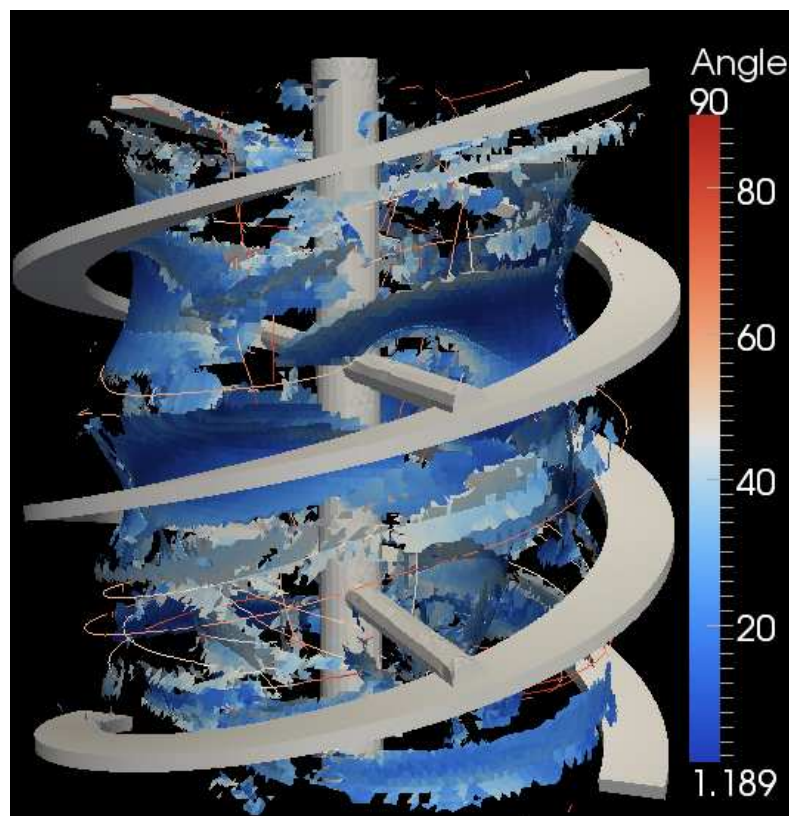


Figure 13: Manifold intersections for the DHR mixer.

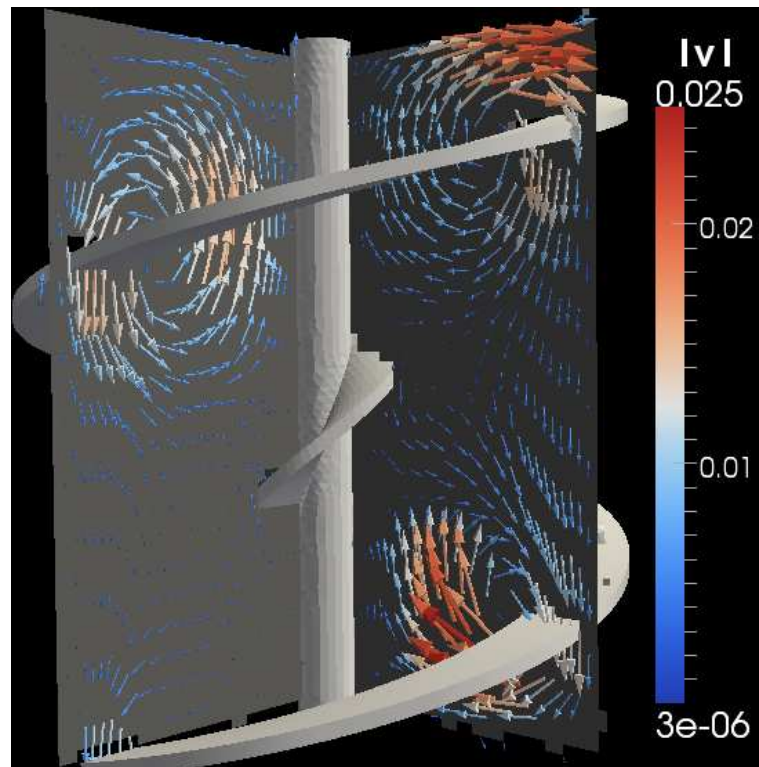


Figure 14: The three-dimensional velocity field on the  $y = 0$  and  $x = 0$  planes for the CSR mixer. The arrows show the velocity components parallel to the planes and are coloured by speed and have length proportional to speed.

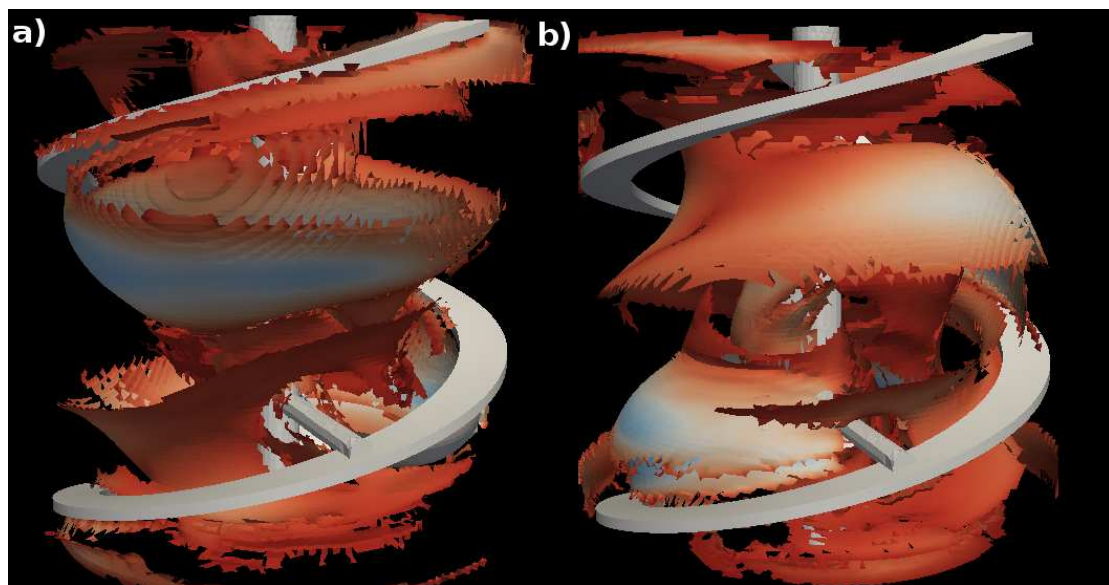


Figure 15: The LCSs for the DHR, a) repelling and, b) attracting. The manifold surfaces are coloured by the strength  $S$  of the manifold with blue indicating a strong sharp ridge in the FTLE field and red a fainter or wider ridge

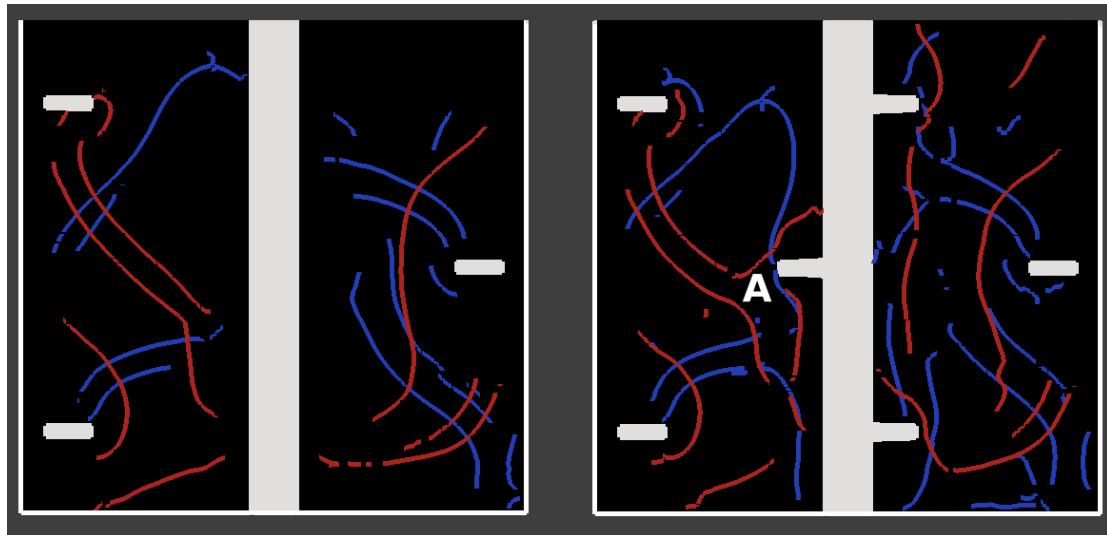


Figure 16: Cross-section of the LCSs for the SHR (left) and the CSR (right). Attracting manifolds are coloured blue and repelling manifolds are coloured red.

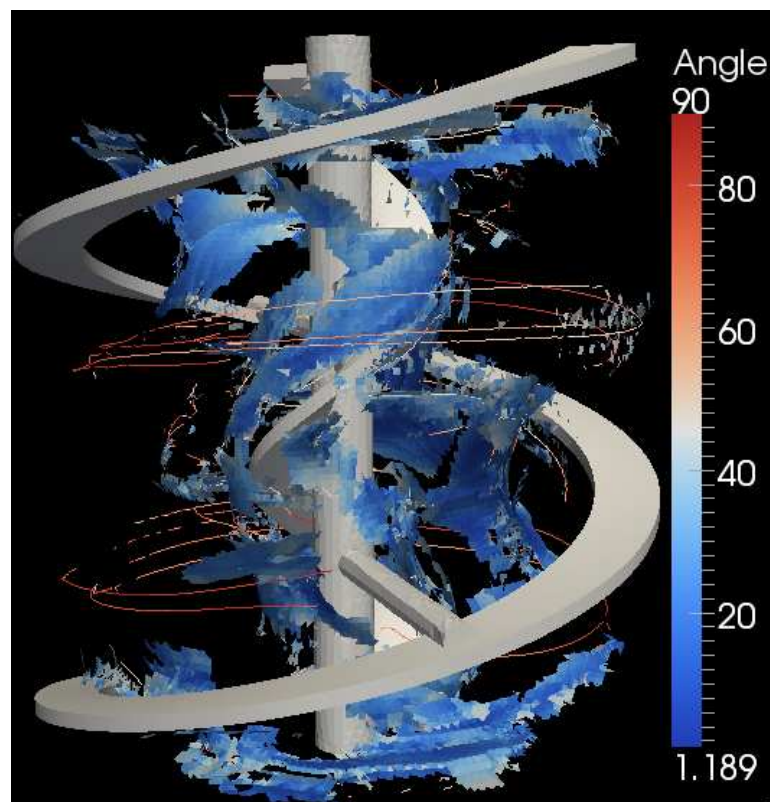


Figure 17: Manifold intersections for the CSR mixer.

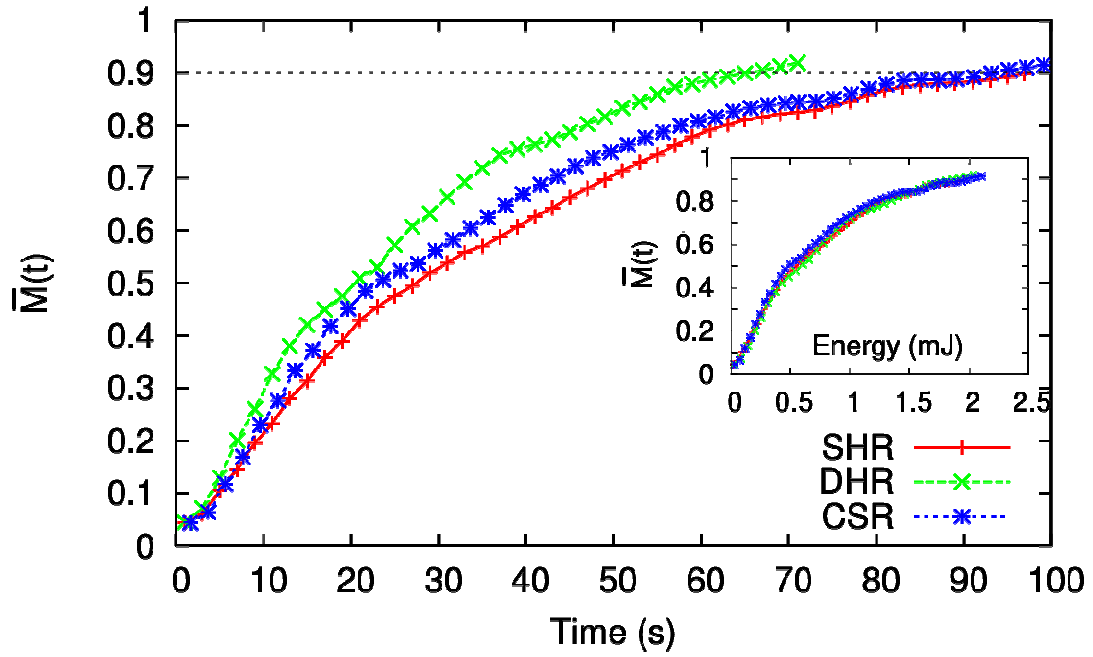


Figure 18: Average mixing measure  $\bar{M}(t)$  showing progress of mixing between fluid initially on either side of the  $x = 0$  plane. Inset:  $\bar{M}(t)$  versus energy used to turn the impellor.

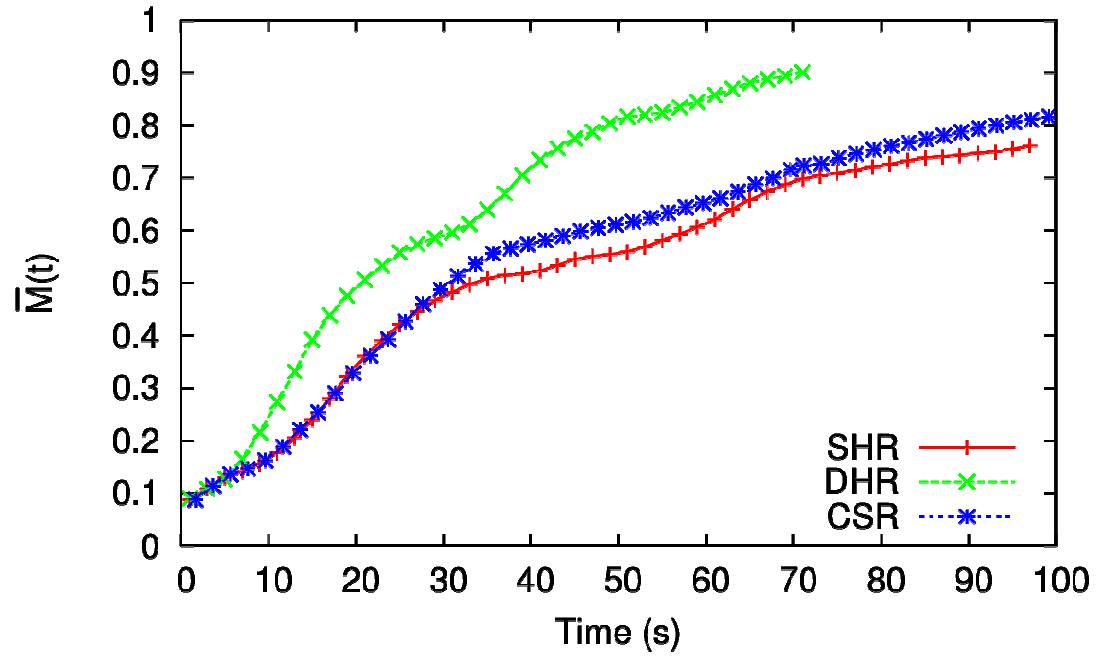


Figure 19: Average mixing measure  $\bar{M}(t)$  between an inner cylinder defined with radius 40 mm and the remaining annular domain outside.

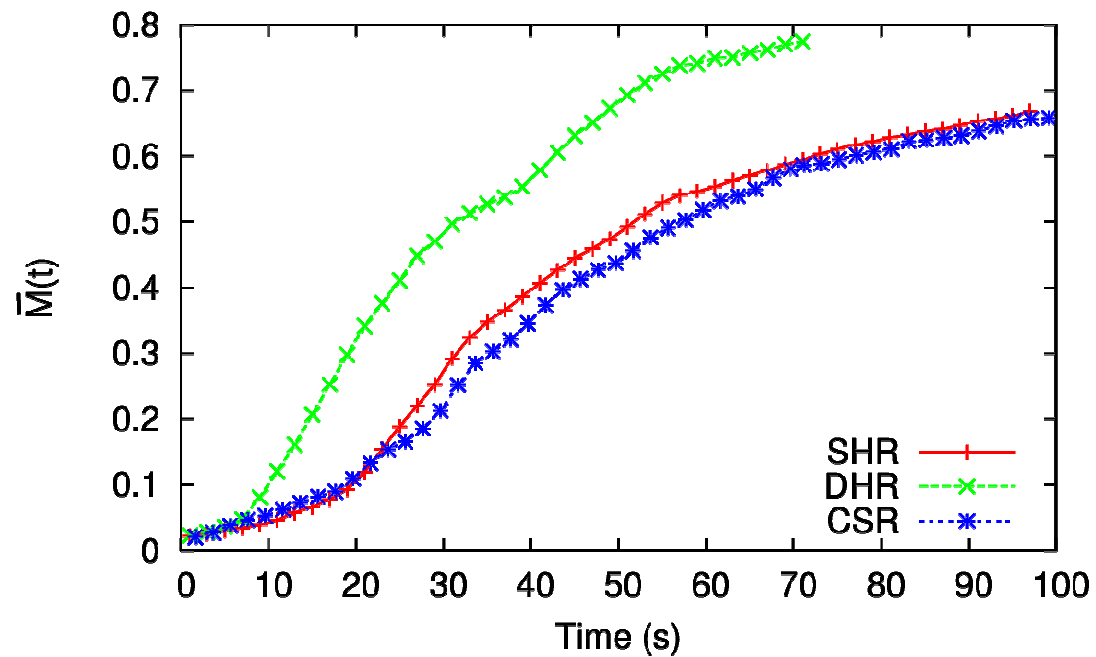


Figure 20: Average mixing measure  $\bar{M}(t)$  between an inner cylinder defined with radius 16 mm and the remaining annular domain outside.

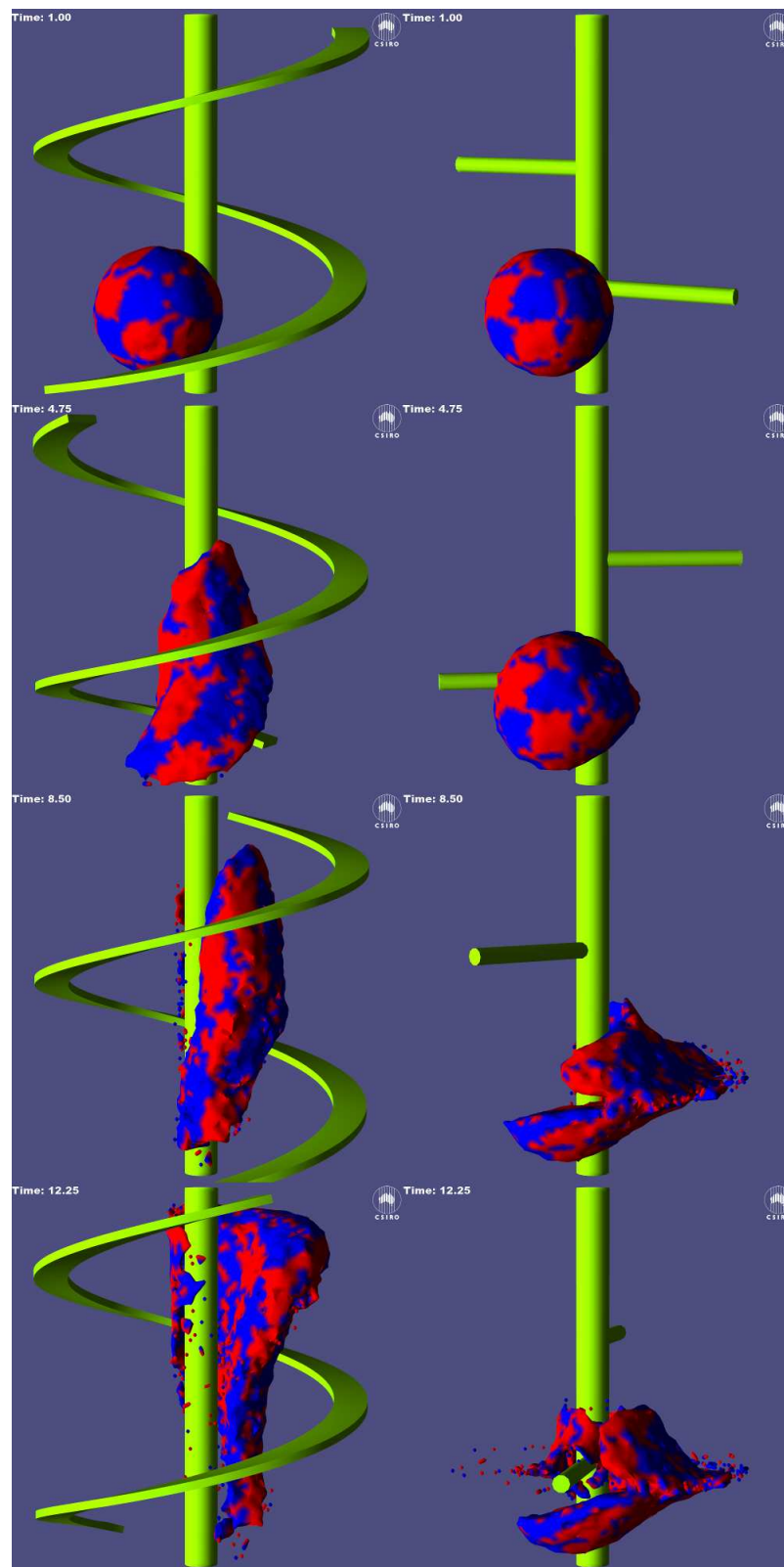


Figure 21: Time sequence showing the transport of an initial sphere of fluid in mixer with only the outer ribbon but no supporting struts (left), and with only the supporting struts but no ribbon (right).

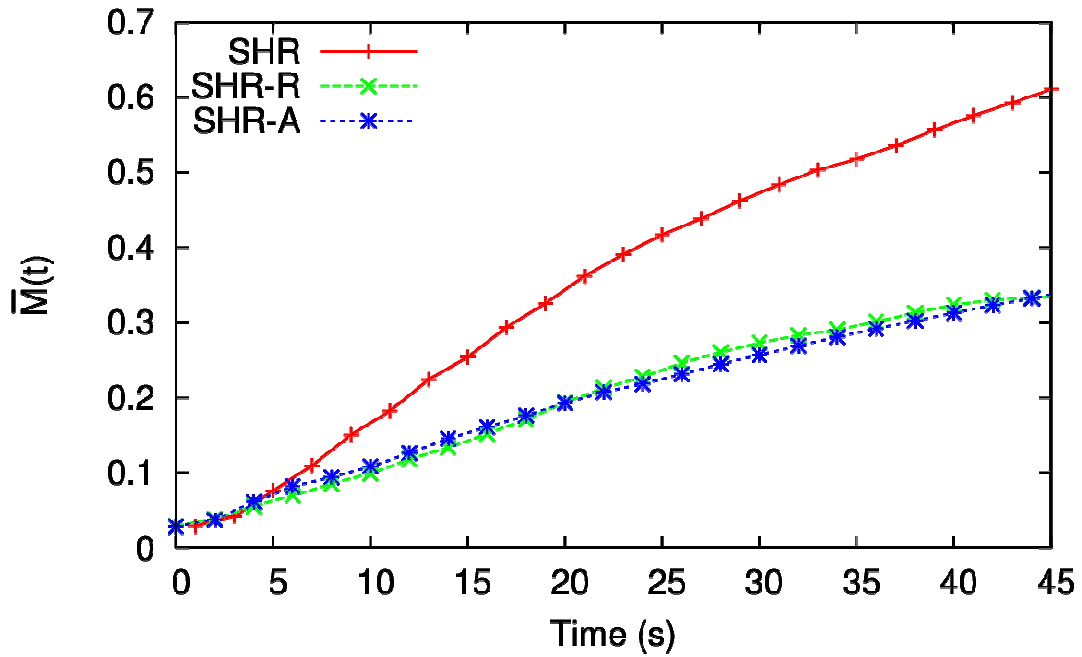


Figure 22: Average measure  $\bar{M}(t)$  showing progress of mixing between fluid initially on either side of the  $x = 0$  plane. Comparison between the SHR and a mixer with only the outer ribbon but no supporting struts (SHR-R), and with only the supporting struts but no ribbon (SHR-A).

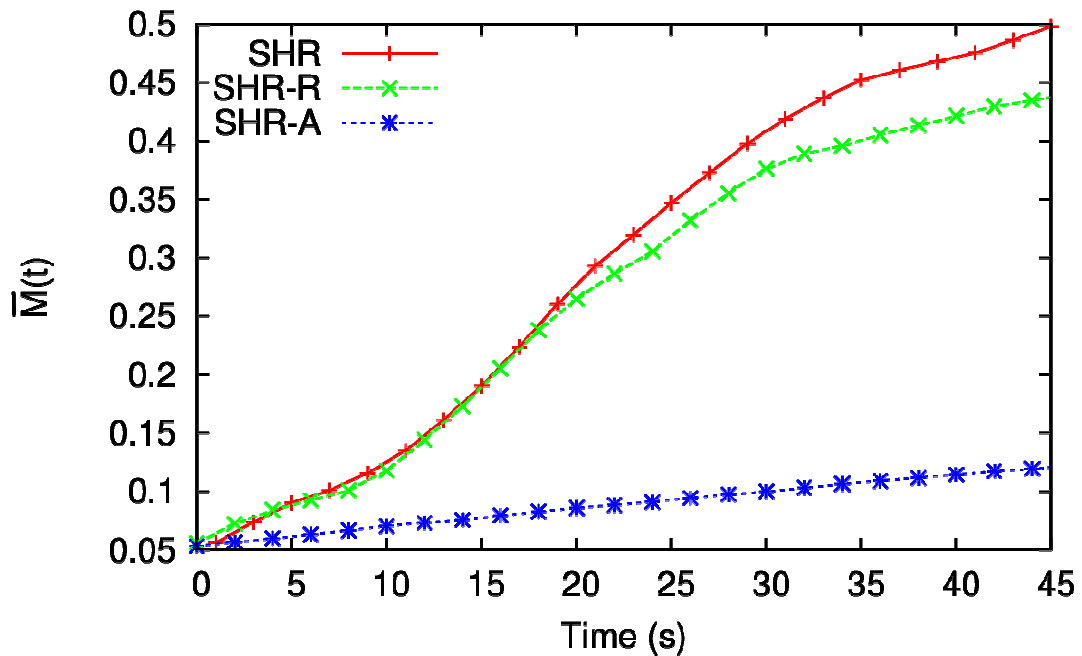


Figure 23: Average mixing measure  $\bar{M}(t)$  between an inner cylinder defined with radius 40 mm and the remaining annular domain outside for the SHR, SHR-R and SHR-A cases.